

PhD degree in Medical Nanotechnology
European School of Molecular Medicine (SEMM)
University of Milan
Settore disciplinare: Fis/03

Novel Platform for Biosensing Application Based on Cluster-Assembled Materials

Elisa Sogne

Centro Interdisciplinare Materiali ed Interfacce Nanostrutturati – CIMAINA

Matricola n. R09371

Supervisor: Prof. Paolo Milani

Dipartimento di Fisica – Università degli Studi di Milano

Anno accademico 2013-2014

Abstract

Rapid methods to identify bacteria in biological samples are important for prompt antimicrobial therapy. The current detection methods are classical biological sample cultures and biochemical tests, which are however, time-consuming and not highly sensitive. A novel and highly performing approach is offered by aptamers acting as recognition elements able to detect epitopes on the surface of a bacterium. Aptamers interacting with specific bacteria are known and then could provide a solid base for developing promising solutions for this issue. With this PhD work I intended to tackle one drawback of aptamer-based biosensor: the lack of platforms for high density aptamers immobilization. Cluster-assembled thin films, have been optimized as supports to demonstrate that aptamers, targeting *Staphylococcus aureus*, well adhere on these substrates and keep their functionality. Moreover, the characteristics of the nanostructured zirconium oxide thin film: thermal stability, good reactivity towards -OH and -COOH groups and nano-morphology, make this material a suitable candidate for the realization of platforms for general screening and biosensing applications. This strategy will offer a promising way for the development of an user-friendly aptamer-based biosensors for screening biological

samples.

Furthermore, I focused on a technological problem, regarding the need of substrates to perform correlative light-electron microscopy (CLEM), designing, developing and testing a device which improve the feasibility of correlative fluorescence/confocal and scanning electron microscopy.

...A chi c'è sempre stato, chi vicino, chi lontano, chi con un sorriso,
chi con uno sguardo, chi con un: “ Sogne! ”, chi con il suo esempio...

Contents

List of Figures	vii
List of Tables	ix
Glossary	xi
1 Introduction	1
1.1 Nanomaterials for biosensing applications	2
1.1.1 Nanoparticles and nanotubes	2
1.1.2 Nanostructured ZrO ₂ for biosensor applications	4
1.2 Case of study: aptamers as bioreceptors	6
1.2.1 Aptasensor targeting <i>Staphylococcus aureus</i>	10
2 Aim of the project	15
3 Materials and Methods	17
3.1 Nanostructured Zirconia fabrication	17
3.1.1 Supersonic Cluster Beam Deposition	17
3.2 Electron beam evaporator	21
3.3 Samples annealing	21
3.4 Nanostructured Zirconia Characterization	21
3.4.1 Atomic force microscopy	22
3.4.1.1 Experimental	24

CONTENTS

3.4.2	X-ray Powder Diffraction	25
3.4.2.1	Experimental	27
3.4.3	Electron Photoemission Spectroscopy	29
3.4.3.1	Experimental	31
3.4.4	High Resolution Transmission Electron Microscopy	32
3.4.4.1	Experimental	33
3.5	Customized aptamer microarrays	33
3.5.1	Aptamers	34
3.5.2	Immobilization of aptamers on nano-structured ZrO ₂	35
3.5.2.1	Nano-structured ZrO ₂ surface functionalization	37
3.5.3	Test of immobilized aptamer activity	37
3.6	Detection of <i>S. aureus</i> -aptamer interaction	38
3.6.1	Fluorescence confocal microscopy	39
3.6.2	Electrophoretic Mobility Shift Assay (EMSA)	39
4	Results and Discussion	41
4.1	Nanostructured Zirconia	42
4.1.1	Morphological Characterization	42
4.1.2	Structural Characterization	48
4.1.3	Spectroscopic Characterization	54
4.2	Aptamer-functionalized nanostructured Zirconia	63
4.3	<i>S. aureus</i> -aptamers interaction	67
4.4	Summary	74
4.4.1	Development of a substrate for aptamer immobilization	74
4.4.2	Aptamer immobilization on zirconia nano-structured substrate	75
4.4.3	Bacteria recognition <i>via</i> immobilized aptamer	76
4.5	Future perspectives	76
5	Appendix	79

CONTENTS

References

85

List of Figures

1.1	Sketch of elements composing a biosensor	5
1.2	Scheme of Systematic Evolution of Ligands by EXponential enrichment (SELEX)	8
2.1	Concept of the Apta-SENSOR device	16
3.1	PMCS scheme	18
3.2	SCBD apparatus	19
3.3	Roughness vs Thickness calibration curve	20
3.4	Schema AFM	22
3.5	Diagram showing the path difference for two beams at angle θ reflected by different planes	26
3.6	Diagram describing the formation of cones of diffraction when performing powder diffraction	27
3.7	The MCX beamline endstation	28
3.8	Sketch of Photoelectric effect	30
3.9	MSB endstation	32
3.10	PSIM protocol	34
3.11	Microarray generation	36
4.1	AFM analysis of nanostructured zirconium oxide surfaces with increasing level of roughness	43
4.2	ns-ZrO _{2-x} surface topographic maps	45
4.3	Evolution of roughness vs thickness	46

LIST OF FIGURES

4.4 TEM images of cluster-assembled zirconia oxide films before and after annealing 47

4.5 Histograms of grain diameters distributions for a cluster-assembled zirconia films before and after annealing 47

4.6 FFT of cluster-assembled zirconia films not annealed 48

4.7 FFT of cluster-assembled zirconia films annealed at 500°C 49

4.8 Diffraction graph of cluster-assembled zirconia showing X-ray intensity as a function of 2-theta angle 50

4.9 Plot of the fraction of monoclinic and cubic crystal phase in function of temperature 51

4.10 Plot of particles size dimension versus temperature 53

4.11 Zr_{3d} core level spectra 56

4.12 C_{1s} core level spectra 57

4.13 O_{1s} core level spectra 58

4.14 VB spectra of cluster-assembled zirconia 60

4.15 VB spectra of the as deposited and water exposed cluster-assembled zirconia films 61

4.16 VB spectra of the as deposited and acetic acid exposed cluster-assembled zirconia films 62

4.17 Aptamer-microarray 63

4.18 Confocal microscopy: XY view spots on ns-ZrO₂ 65

4.19 Confocal microscopy: Z view spots on ns-ZrO₂ 66

4.20 Confocal microscope images of Bacteria 68

4.21 Confocal microscope images of Bacteria 69

4.22 Confocal microscopy: Z-axis view of bacteria 69

4.23 SA23 aptamer-Bacteria interaction 70

4.24 SA17 aptamer-Bacteria interaction 71

4.25 Comparative analysis of 3 different *S. aureus* strains 72

List of Tables

3.1	XPS samples tested	31
3.2	Aptamers tested - Sequences, size, labelling, modification.	35

Glossary

AFM	Atomic force microscope
BSA	Bovin serum albumin
CCD	Charged coupled device
CLEM	Correlative light electron microscopy
CNT	Carbon nanotube
CPS	Counts per seconds
DNA	Deoxyribonucleic acid
EDTA	Ethylene diamine tetra acetic acid
EMSA	Electrophoretic mobility shift assay
FFT	Fast Fourier transform
HPLC	High performance liquid chromatography
HRTEM	High resolution transmission electron microscope
LOD	Limit of detection
MCX	Material characterization by X-ray
MSB	Material science beamline
NIST	National Institute of Standards and Technology

GLOSSARY

NMO	Nanostructured metal oxide
PAA	Polyacrylic acid
PBS	Phosphate-buffered saline
PBSM	PBS 1X + 5 mM MgCl ₂
PBSMT	PBS 1X + 5 mM MgCl ₂ + 0.1% (V/V) Tween20
PLD	Pulsed laser deposition
PMCS	Pulsed microplasma cluster source
PoC	Point of care
PS	Photoemission spectroscopy
PSIM	Protein surface interaction microarray
RNA	Ribonucleic acid
SAM	Self assembled monolayer
SAU	<i>Staphylococcus aureus</i>
SCBD	Supersonic cluster beam deposition
SELEX	Systematic evolution of ligands by exponential enrichment
SMP	Sample
SPR	Surface plasmon resonance
SWCNT	Single wall carbon nanotube
TBE	Tris/Borate/EDTA
TEG	Triethyleneglycol
TEM	Transmission electron microscope

GLOSSARY

UHV	Ultra high vacuum
UPS	UV-photoemission spectroscopy
VB	Valence band
XPS	X-ray photoemission spectroscopy
XRPD	X-ray powder diffraction

1

Introduction

Nanotechnology, with the development of tools and processes used to fabricate, measure and image nanoscale objects, is playing an important role in the progress of biosensing where the main demands are for high sensitivity, high specificity and fast response (1). In recent years biosensors have become important and practical tools in the field of healthcare, chemical and biological analysis, environmental monitoring, food safety control, and homeland security. Early detection increases the probability of curing diseases and significantly decreasing the rate of mortality. However, many of the conventional test methods currently available are slow, require large amounts of sample materials and may lead to false positive or negative results. Therefore, there is a demand for tools able to give fast and reliable responses.

1. INTRODUCTION

1.1 Nanomaterials for biosensing applications

Nanomaterials can be generally defined as materials with at least one dimension in the size range of 1-100 nm. Operating at a length scale of one-billionth of a meter, the properties of nanomaterials are significantly different from the bulk due to the high surface-to-volume ratio (2).

The increased sensing surface and strong binding properties can be exploited to improve the sensitivity of the detection system whether based on solid nanostructured supports or based on the use of nano-objects (e.g. nanoparticles, nanorods, nanotubes, etc.) for biosensing applications. Thus, over the last fifteen years, efforts have focused on the use of nanotechnology to develop nanostructured materials (e.g. graphene and ZnO nanowires, mesoporous silica-based materials, nanotubes, nanowalls and nanorods, nanoparticles, etc.) as biomolecule immobilizing matrices/supports to improve biosensing performance (1, 3).

1.1.1 Nanoparticles and nanotubes

Nanoparticle-based biosensors are particularly attractive because they can be easily synthesized in bulk using standard chemical techniques, and do not require advanced fabrication approaches (4). They also offer particularly high surface areas due to their extremely small size and are typically used as suspensions in solutions (during the time when they interact with the analyte). Most biological molecules can be labelled with metal nanoparticles without compromising their biological activities (5). One example is the use of gold nanoparticles (6) due to their biocompatibility, their optical and electronic properties, and their rela-

1.1 Nanomaterials for biosensing applications

tively simple production and modification (7). In fact these metal nanoparticles are extensively used in surface plasmon resonance biosensor (SPR): this method is usually based on the change of the dielectric constant of propagating surface plasmons' environment of gold films where the detection of the analyte can be recorded in different ways like the changes of the angle, intensity, or phase of the reflected light (8, 9). This phenomenon is strongly dependent on the size, shape of the nanoparticle and the dielectric constant of its environment (10). The environmental dependency represents a great advantage for (bio)-analytics since the recognition event can result in a change of the oscillation frequency and therefore to a color change of the gold nanoparticles observable with the naked eye. Taking advantage of these properties a wide series of efficient colorimetric biosensors were developed for DNA or oligonucleotide detection, or immunosensors (11, 12, 13, 14). Magnetic nanoparticles are frequently used as alternatives to fluorescent labels in biosensor devices. A relevant advantage of using magnetic nanoparticles is the possibility to concentrate the analyte before the detection event. Magnetic nanoparticles functionalized with a bioreceptor can simply be mixed with the analyte solution and interacts specifically with the target. After applying an external magnetic field, the nanoparticles agglomerate and can be separated from the solution. Efficient isolation of DNA strands in complex media was achieved in a fast and efficient manner using silica or gold coated core/shell nanoparticles (15, 16, 17). The use of magnetic nanoparticles for labeling is particular interesting for biosensing applications since biological entities do not show any magnetic behavior or susceptibility and, therefore, no interferences or noise is to be expected during signal capturing (18). An ultra-high sensitive magnetore-

1. INTRODUCTION

sistant biosensor was developed for *Escherichia coli* (19) detection or Salmonella identified in skimmed-milk samples with a limit of detection (LOD) of 1 colony forming-unit (cfu)/mL using a magneto-genosensing setup (20). Another example of nanomaterials devoted to biosensing are carbon nanotubes (CNTs). In particular, carbon nanotubes possess the outstanding combination of nanowire morphology, biocompatibility and electronic properties (21). Therefore, carbon nanotube interfaces present enhanced capacities, e.g. to approach the active sites of a redox enzyme and to wire it to the bulk electrode. Furthermore, their ease and well documented organic functionalization (22) brings new properties to nanostructured electrodes such as specific docking sites for biomolecules or redox mediation of bioelectrochemical reactions. Moreover, CNT films exhibit high electroactive surface areas due to the natural formation of highly porous three-dimensional networks, suitable for the anchoring of a large amount of bioreceptor units, leading consequently to high sensitivities (23, 24).

1.1.2 Nanostructured ZrO₂ for biosensor applications

A biosensor is a self-contained integrated device which is capable of providing selective quantitative analytical information using a biological recognition element which is in direct spatial contact with a transducer element ¹. Hence the performance of biosensors depends on their components (see figure 1.1). One important element is the matrix material (i.e. the layer on which are immobilized the recognition biomolecule and transducer), acting a crucial role in defining the stability, sensitivity and shelf-life of a biosensor (25).

¹According to the definition of International Union of Pure and Applied Chemistry (IUPAC)

1.1 Nanomaterials for biosensing applications

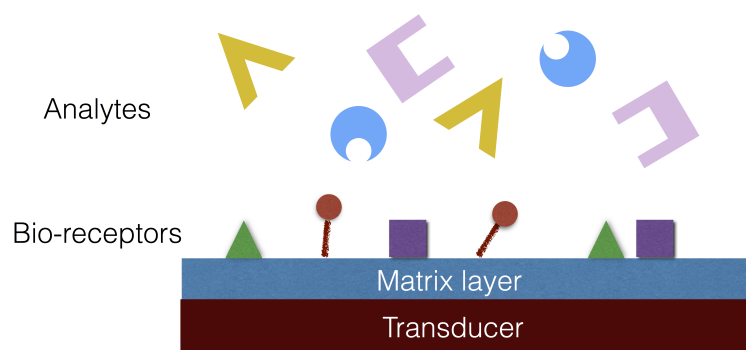


Figure 1.1: Sketch of elements composing a biosensor - Analytes are the target of the detection, bio-receptors are the biological component which interact with the analytes and the matrix layer is the physical interface, between transducer and biological components, on which bio-receptors are immobilized. The transducer is the component that transform the signal coming from the interaction between analytes and bio-receptors into another signal that can be measured and processed.

Among the various types of nanomaterials that have been developed (polymers, metal nanoparticles, self-assembled monolayers (SAMs), etc.) for biological applications, nanostructured metal oxides (NMOs) have recently aroused much interest as immobilizing matrices for biosensor development (26, 27, 28, 29). Nanostructured oxides of metals such as zinc, iron, cerium, tin, zirconium and titanium have been found to exhibit interesting nanomorphological, functional biocompatible and non-toxic properties. These materials exhibit enhanced electron-transfer kinetics and strong adsorption capability, providing suitable microenvironments for the immobilization of biomolecules (30). Different methods have been used for the fabrication of NMOs structures, including solgel methods for the production of three-dimensional (3D) ordered rough nanostructures (28, 31), radiofrequency

1. INTRODUCTION

sputtering for rough nanostructures (27), pulsed-laser deposition (PLD) (32), nanoparticles self-assembly (33). The controlled preparation of a nanostructured metal oxide is considered to play a significant role in the development of biosensors. Nanostructured zirconia nanoparticles and films have recently been considered as a potential solid support for the immobilization of bioactive molecules in biosensor applications, due to their high thermal/mechanical/chemical resistance, excellent biocompatibility, and their affinity towards groups containing oxygen (30). During the past few years, both functionalized and unfunctionalized zirconia nanoparticles have been developed as solid supports for enzyme immobilization and biocatalysis (34). For example, to immobilize hemoglobin for a novel hydrogen peroxide biosensor (35, 36), to immobilize DNA for investigating the effects of lanthanide on its electron transfer behavior, for the detection of DNA hybridization (37), to detect urea (38) and to detect electrochemically glucose (39). These examples show how the application of nanostructured zirconia as a support for biosensors is a growing field. In particular since our group has the knowledge to fabricate nanomaterials, by the deposition of nanometric cluster, characterized by a random nanoscale roughness, I took advantage of this expertise to develop a cluster-assembled nanostructured zirconia thin film ($ns\text{-ZrO}_x$) for the realization of a platform suitable for biosensing applications.

1.2 Case of study: aptamers as bioreceptors

The case studied in this work presents the use of aptamers as bioreceptors for the targeting of *Staphylococcus aureus*. Theoretically, the recognition component

1.2 Case of study: aptamers as bioreceptors

is the key for the sensor performance. An ideal recognition component should possess the characteristics of high sensitivity, admirable selectivity, fast response, robust performance and versatility for various targets. With these criteria, antibodies and aptamers are two of the mostly used recognition components (40). Antibodies, responding to specific antigens, have been widely applied in the construction of various sensors. However, as a functional protein, an antibody is sensitive to its environment and its activity is unstable. Despite the large use of enzymes and antibodies in biosensing (41, 42), aptamers, since their discovery in 1990 by both Gold's group and Szostak's group (43, 44), have been used in a wide variety of applications in either basic research or, especially, health-related diagnostics and therapeutics (45, 46, 47) and are becoming an alternative to antibodies.

Aptamers are small single-stranded DNA (ssDNA) or RNA oligonucleotide segments, which bind to their targets with high affinity and specificity via unique three-dimensional structures. Aptamers are identified through an *in vitro* selection process called Systematic Evolution of Ligands by EXponential enrichment (SELEX) (figure 1.2) which specifically isolates aptamers for a target of interest involving iterative rounds (48).

In a SELEX process, in general (figure 1.2 **a**), a random aptamer or oligonucleotide library pool (DNA or RNA) is incubated with the target of interest, with heating and cooling to promote formation of stable structures. After washing, the bound sequences are eluted and incubated with a control target (if negative selection is required) to remove sequences that exhibit recognition with the control as well. The protein-bound aptamers are then recovered. These sequences

1. INTRODUCTION

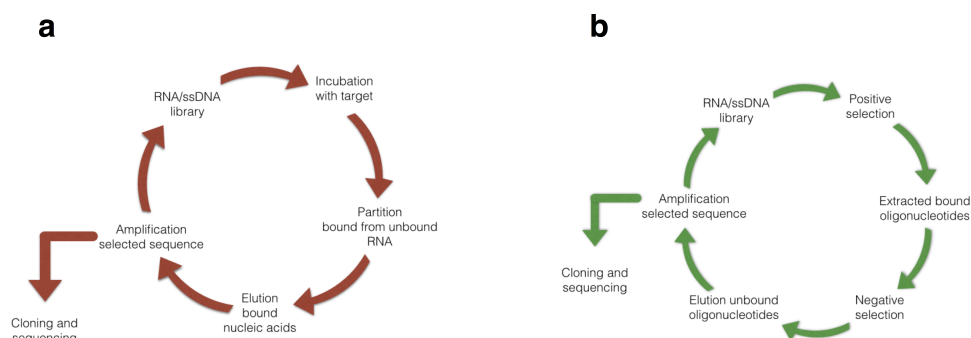


Figure 1.2: Scheme of Systematic Evolution of Ligands by EXponential enrichment (SELEX) - In **a** a general SELEX process. In **b** a SELEX process adapted to target cells. Figures adapted from (49).

are amplified with PCR or reverse transcription-PCR. ssRNA or DNA sequences representing the recovered sequences are then generated from these PCR products and used in the subsequent selection round. The process is repeated until the pool is enriched for sequences that specifically recognize the target. The enriched pool is cloned and then sequenced to obtain the individual sequences known as the aptamer. While in Cell-SELEX (figure 1.2 **b**), living cells are used as targets to generate aptamers that specifically recognize cells, starting from a library of ssDNA. This library, which has a random sequence of 30-40 bases and a region flanked by primer sequences of 18-20 bases, is incubated with the target cells. The library and forward primers are labeled with a fluorophore, so that the sense strand of the PCR product for each round, which serves as the library for the next round, is also fluorescently labeled, enabling the entire process to be monitored by flow cytometry. After washing, the DNA sequences bound to the target cell surface are collected and then incubated with the negative control cells. All the

1.2 Case of study: aptamers as bioreceptors

DNA sequences that bind to the negative control cells are removed. To avoid recognition of normal cells, the aptamers bound to these nonspecific proteins are removed. The remaining sequences are amplified for the next round of selection. Generally, about 20 rounds of Cell-SELEX are required to isolate aptamers with the highest selective affinity to the target cells (45).

The aptamer's high affinity is attributed to the remarkable dissociation constants (K_d) ranging from picomolar to nanomolar levels between aptamer and its target (50). The excellent selectivity derived from the reason that aptamer can distinguish even minor structural differences between targets and their analogs (51).

Advantages in using aptamers:

- Aptamers can bind with a broader range of targets, including metal ions, amino acids, other small organic molecules, viral proteins, even cells and bacteria (52, 53, 54, 55)
- Aptamers can be successfully obtained from synthetic chemicals with characteristics of higher purity and lower costs.
- Aptamers can be flexibly modified with various chemical tags including fluorescence probes, electrochemical indicators and nanoparticles.
- Aptamers are small in molecular weight and more stable maintaining the same characteristics after repeated steps of denaturation and renaturation.

These unique characteristics make aptamers an ideal recognition element for biosensors.

1. INTRODUCTION

1.2.1 Aptasensor targeting *Staphylococcus aureus*

Aptasensors are aptamer-based biosensors with excellent recognition capability towards a wide range of targets (40). As said before, the case of study of this PhD work is the development of a platform for immobilization of aptamers targeting *S. aureus*. *Staphylococcus aureus* is a common pathogen found on human skin and into human respiratory tract. It is a Gram positive coccus, presenting the typical bacterial structure except flagella and it has been recognized as an opportunistic pathogen. *S. aureus* infections are often acute and pyogenic, involving the skin and postoperative wounds and, if not adequately treated, they may spread to surrounding tissue or via bacteremia to metastatic sites, thus involving other organs, inducing pneumonia, osteomyelitis, acute endocarditis, meningitis and abscesses. The prognosis of these infections is dramatically worsened when the etiological agent is resistant to methicillin. For this reason, there is currently a huge demand for rapid methods to detect *S. aureus* with the potential to be incorporated into point-of-care (PoC) diagnostic systems (56). Conventional methods to detect *S. aureus*, such as biochemical assays, always require the growth of bacterial cells, at least one day, for bacterial identification delaying the diagnosis.

Since the final aim of this PhD work is the development of a platform suitable for aptamers immobilization to detect *Staphylococcus aureus*, in this introduction we will focus mainly on aptasensor targeting this bacteria. A first report of aptamers used as bio-recognition elements against *S. aureus* is reported by Cao *et al.* (53). In this paper, a panel of ssDNA aptamers specific to *S. aureus* was obtained by a whole bacterium-based SELEX procedure and applied to probing *S. aureus*.

1.2 Case of study: aptamers as bioreceptors

After several rounds of selection with *S. aureus* as the target and *Streptococcus* and *S. epidermidis* as counter targets, the highly enriched oligonucleic acid pool was sequenced and then grouped under different families on the basis of the homology of the primary sequence and the similarity of the secondary structure. Eleven sequences from different families were selected for further characterization by confocal imaging and flow cytometry analysis. Results showed that five aptamers demonstrated high specificity and affinity to *S. aureus* individually. The five aptamers recognize different molecular targets by competitive experiment. Combining these five aptamers had a much better effect than the individual aptamer in the recognition of different *S. aureus* strains. In addition, the combined aptamers can probe single *S. aureus* in pyogenic fluids. Their work demonstrated that a set of aptamers specific to one bacterium can be used in combination for the identification of the bacterium instead of a single aptamer (53). Starting from the assumption that the aptamers developed in Cao's work were specific for *S. aureus*, we decided to use these aptamers as biorecognition elements immobilizing them onto the cluster-assembled zirconium oxide thin films developed during this PhD project. In another work by Zelada-Guillen (56) in 2012, a first example of biosensor able to detect *Staphylococcus aureus* in real-time has been reported. The biosensor is based on a network of single-walled carbon nanotubes (SWCNTs) acting as an ion-to-electron potentiometric transducer and anti-*S. aureus* aptamers are the recognition element. Carbon nanotubes were functionalized with aptamers using two different approaches: first non-covalent adsorption of drop-casted pyrenil-modified aptamers onto the external walls of the SWCNTs; second covalent bond formation between amine-modified aptamers and carboxylic

1. INTRODUCTION

groups previously introduced by oxidation at the ends of the SWCNTs. Both of these approaches yielded functional biosensors but there were large differences in the minimum detectable bacteria concentration and sensitivity values. They demonstrated that potentiometric biosensors based on single-walled carbon nanotubes as ion-to-electron transducers and aptamers as recognition elements, are excellent biosensors for "real-time" and "label-free" detection of *S. aureus* as they improve on all the current detection methods for this pathogen. Otherwise the biosensor performance parameters depending on the functionalization approach employed during the biosensor construction demonstrate how the immobilization step is crucial for the development of a highly sensitive biosensor. A more recent example by Chang *et al.* (52) in 2013, shows a rapid, ultra-sensitive, low cost, and non-polymerase chain reaction (PCR)-based method for bacterial identification. The method is based on the measurements of the resonance light-scattering signal of aptamer-conjugated gold nanoparticles. Thanks to this method they detected single *S. aureus* cell within 1.5 hours. What is missing in the field of aptasensor targeting *Staphylococcus aureus*, is a support for high density and functional surface immobilization of aptamers, besides a user-friendly read-out of the detected molecules which can be easily implemented into a low-cost, high-throughput, multiplexed clinical diagnostic point-of-care device (PoC). In general, more attention should be paid to understand the mechanism behind the molecules interaction with surfaces in order to design materials with specific chemical and physical properties affecting the immobilization in the desired way. In this *scenario* biomaterial arrays, based on the production of a large material library in a microarray format, are used for finding the material with the best performance

1.2 Case of study: aptamers as bioreceptors

for a specific application, such as the realization of substrates for the functional immobilization of enzymes or the synthesis of antifouling surfaces. This approach can also be used as a fast pre-screening step for the selection of nanostructured materials for applications in the fields of *in vitro* cell culture, tissue engineering or implants, allowing the identification of the best surface among those of the library that adsorbs proteins that promote cell adhesion and differentiation such as integrins or growth factors. The material developed in this work can be easily implemented into a platform for high-throughput screening of whatever the nanostructured surfaces (being the technique used for the material fabrication able to control nanoscale morphology independently from surface chemistry) for bioreceptor immobilization or the immobilization conditions used. In fact, this material, combined with microarray technology improve the definition of the optimal conditions (e.g. pH, salt concentration, bioreceptor concentration, etc.) for immobilizing bioreceptor on nanostructured surfaces (57, 58). Part of this PhD work has been carried on, within the CARIPLO's project: "Development of an innovative user-friendly colorimetric biosensor based on aptamer-functionalized nanomaterials for the detection of *Staphylococcus aureus* from different biological source", at Fondazione Filarete, Milan, Italy. The final goal of the CARIPLO's project is the development of a new user-friendly detection system, for the rapid targeting of *S. aureus*, based on a colorimetric system switching in the visible region in order to not require any expensive detection system and be so potentially available for a point-of-care (PoC) diagnostic system.

In the first chapter an overview of the use of nanomaterials in biosensing application is discussed. Moreover an example of nanomaterials applied on biosensing

1. INTRODUCTION

of *Staphylococcus aureus* is given, focusing on the aptamer as the bioreceptor element. In the second chapter the goal of the project is described. In the third chapter the techniques used for the fabrication, characterization and implementation of the material developed in this work, as biosensing platform, are described. In the fourth chapter the presentation of results and their discussion is the focus. In addition to the project for the realization of a sensor for bacterial detection I have been involved in the development of a device for Correlative Light-Electron Microscopy (CLEM). In particular my task consisted of the design and fabrication of a support suitable for both confocal microscopy and scanning electron microscopy (SEM). This will be described in detail in the Appendix.

2

Aim of the project

The aim of this PhD project was the realization and characterization of a platform, based on cluster-assembled nanomaterials, suitable for a biosensing applications. The proof of concept to demonstrate the feasibility of this platform for this purpose has been conducted immobilizing aptamers for the development of a biosensor targeting *S.aureus*.

2. AIM OF THE PROJECT

The concept, behind the idea to realize a new user-friendly and cheap biosensor targeting *S. aureus*, is to immobilize, on a nanostructured support, aptamers hybridized with labeled-peptides that could be displaced in the presence of *S. aureus* inducing a colorimetric switch in the visible region (see figure 2.1).

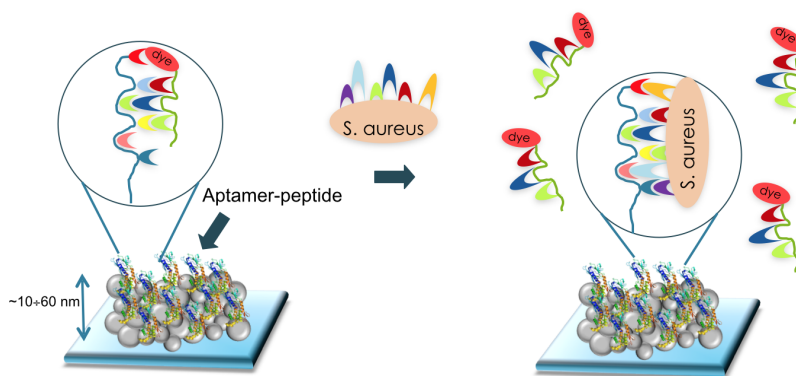


Figure 2.1: Concept of the Apta-SENSOR device - The idea is to immobilize aptamers hybridized with labeled-peptides on a nano-structured support. Since bacteria have a higher affinity towards aptamers, their presence, in the biological sample, displaces the peptides which going in solution, induce a colorimetric switch.

3

Materials and Methods

3.1 Nanostructured Zirconia fabrication

3.1.1 Supersonic Cluster Beam Deposition

Nanostructured thin films were grown on glass microscope slides by depositing a supersonic seeded beam of ZrO_{2-x} clusters produced by a pulsed microplasma cluster source (PMCS) under high vacuum conditions. Figure 3.1 shows a schematic representation of the deposition apparatus consisting of two differentially pumped vacuum chambers separated by a gate.

Cluster beam deposition process consists of the following main steps:

- Clusters are produced in the cluster source by plasma condensation
- Clusters are then extracted from the source and a seeded beam is produced
- Clusters are deposited on the substrate

3. MATERIALS AND METHODS

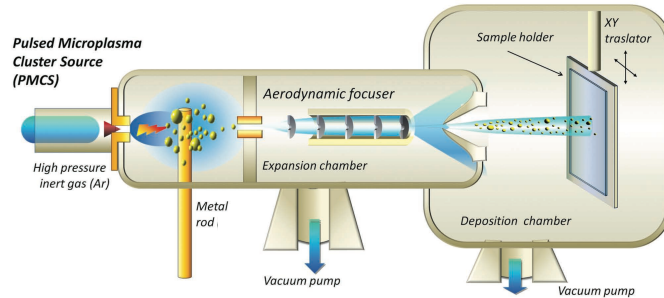


Figure 3.1: PMCS scheme - Schematic view of the apparatus used for SCBD (not to scale)(59)

The source (PMCS), located in the first chamber called "expansion chamber", is composed by a ceramic hollow body inside of which is obtained a cylindrical cavity (volume of few cm^3) at whose end there is a solenoid pulsed valve which regulates the inlet of an high pressure gas (see Figure 3.2). The opposite end is connected to the second chamber (called "deposition chamber") through a low conductance nozzle and it represents the cluster beam exit. In the cavity of the source is insert a cylindrical zirconium rod.

The source works in a pulsed regime and every cycle of work is a four-step process:

1. Introduction in the source cavity of a pulsed Argon delivered by the solenoid valve (pulse duration of the order of hundreds of microseconds, pressure of 40 bar, typical repetition rate 2-4 Hz)
2. Ignitium of an argon plasma by applying a voltage between the electrodes (voltage 850 V)

3.1 Nanostructured Zirconia fabrication

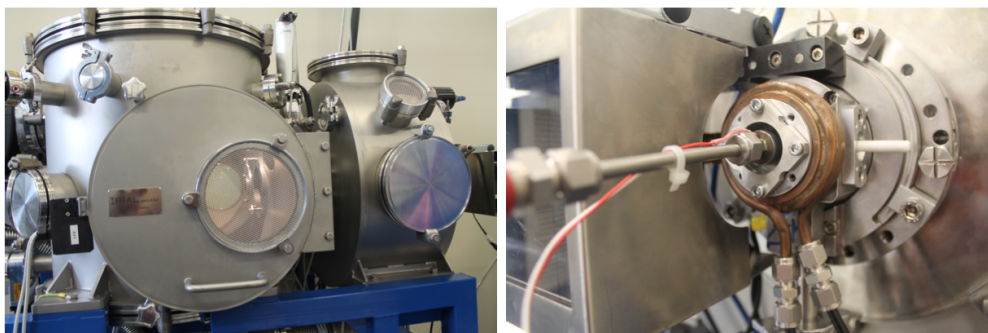


Figure 3.2: SCBD apparatus - On the left the deposition machine composed by the deposition chamber and the expansion chamber. On the right a detail of the gas inlet.

3. Sputtering of the cathode and condensation of cluster
4. Extraction of the nanoparticles by carrier gas expansion through the nozzle and formation of a seeded supersonic beam

The PMCS operation principle is based on the ablation of the zirconium cathode, continuously rotated by means of an external motor in order to allow constant ablation conditions for all pulses and a homogeneous consumption of the rod, by an argon plasma jet ignited by a pulsed electric discharge. After the ablation, ZrO_{2-x} ions thermalize with argon and condense to form clusters. The mixture of clusters and inert gas is then extracted in vacuum through a nozzle to form a seeded supersonic beam, which is collected on a substrate located in the beam trajectory. The use of supersonic beams of cluster allows a stronger control of the cluster mass distribution and kinetic energy with the possibility to obtain very high deposition rates (60) and very collimated beams (61). With this technique it is possible to control the roughness of the deposited thin films by changing

3. MATERIALS AND METHODS

the thickness of the material deposited since the two parameters (thickness and roughness) are correlated by the calibration curve shown in Figure 3.3.

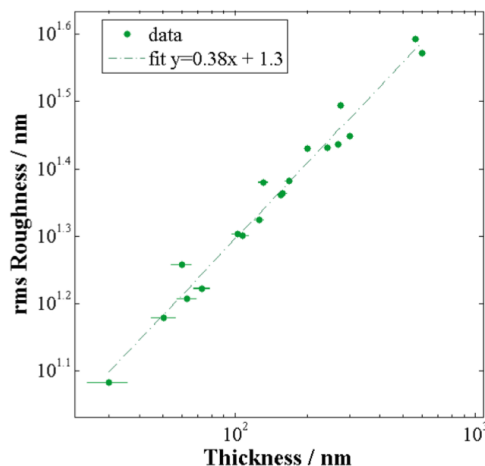


Figure 3.3: Roughness vs Thickness calibration curve - Log-log plot of the evolution of roughness with ns-ZrO₂ film thickness at room temperature and the corresponding linear fit (62).

Exploiting simple aerodynamic effects one can control the divergence of the supersonic beam and the mass distribution of the particles in it (63). By using very collimated beams, high deposition rates can be achieved, moreover, simply by using stencil masks placed in contact with the substrate, patterned films with very high lateral resolutions can be obtained making this technology compatible with the other planar microtechnologies (63). Since clusters have low kinetic energies, well below the binding energy of atoms in the aggregates, when they impact on the surface there is no substantial fragmentation and the deposited film retains a memory of the structure the cluster had in the gas phase (64).

3.2 Electron beam evaporator

Flat thin films were grown on glass microscope slides by depositing zirconium by a conventional custom-made evaporation system, the pressure inside the deposition chamber was brought to 6.0×10^{-6} mbar. The beam was switched on and set to a voltage of 6 kV, and the evaporation was started by gradually increasing the current to 165 mA, a value at which zirconium (99.999% pure, Kurt J. Lesker, Hastings, UK) starts to melt, evaporate and deposit at a rate of 0.2 Å/sec.

3.3 Samples annealing

To study the influence of temperature on the morphology and crystal structure of cluster-assembled thin films, we performed an annealing in a oven with a controlled dry-air flux following a ramp of 50°C in 5 min and then heating the sample at fixed temperature for 2 hours.

3.4 Nanostructured Zirconia Characterization

This part will describe different morphological, structural and spectroscopic characterization techniques used in this thesis, including atomic force microscopy (subsection 3.4.1), x-ray diffraction (subsection 3.4.2), high-energy resolution photoemission spectroscopy (subsection 3.4.3) and high-resolution transmission electron microscopy (subsection 3.4.4).

3. MATERIALS AND METHODS

3.4.1 Atomic force microscopy

The atomic force microscope (AFM) is a high resolution scanning probe tool to determine direct images of material surfaces as well as details about film roughness. To obtain the topography images the AFM uses the interaction between a small tip and the sample surface. Figure 3.4 shows the design of a standard AFM system.

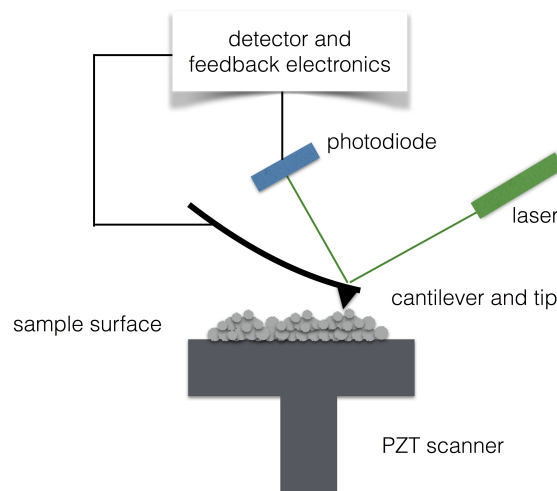


Figure 3.4: Schema AFM - Sketch of AFM microscope composed by a piezoelectric scanner where the sample is placed; a cantilever ending with a nanometre tip; a laser beam impinging the cantilever and a photodiode, divided into four quadrants, to register the cantilever deflection and the systems for feedback control.

The sample is mounted on a piezoscanner responsible for the movements in the x, y and z directions. The tip is attached on a cantilever and it is generally made out of silicon or silicon nitride with a nominal radius of 5-10 nm. During the measurement, the tip moves at few hundred angstroms over the surface or even slightly touches it. An interaction force between the tip and the surface

3.4 Nanostructured Zirconia Characterization

leads to a deflection of the cantilever. This deflection of the cantilever is detected optically. A laser beam is reflected on the tip surface and hits the photodetector which consists of a four-section split photodiode able to detect displacements of the laser beam of 10 Å. Monitoring the difference between opposite diodes, the knowledge of the distance proportion between the tip and the detector and the length of the cantilever allows a quantification of movements at the Angstrom scale. The difference of the top and bottom diodes identifies the torsion of the tip. These mechanical movements are transformed into electric signals. The use of appropriate software allows real topography images of the sample surface to be created. There are two basic modes of operation: the contact or the tapping mode. Each mode uses different physical effects for surface analysis. In the contact mode, the tip actually makes physical contact with the surface. The tip is approached to the sample until the interactions between the tip and the sample cause the bending of the cantilever. In this way the cantilever deflection is measured while the tip is scanning through the sample. In the non-contact mode (tapping mode), an oscillation of the cantilever is produced near the sample's surface (typically 10-100 Å). This mode has the advantage of lowering the possible sample contamination and reducing the tip damage. On the other hand, the force registered will be some orders of magnitude lower than in contact mode. The cantilever is vibrated at a frequency close to its resonance (on the order of hundreds of kHz); when it is approached to the sample, changes in the resonance frequency or in the oscillation amplitude are registered. At the same time, the phase lag between the input oscillation signal and the cantilever output can be recorded. This phase lag is used to monitor changes in the mechanical properties

3. MATERIALS AND METHODS

of the sample surface, detecting regions with different adhesion or friction. This information can, in some cases, be connected to chemical changes in the sample surface.

3.4.1.1 Experimental

The investigation of the morphology of the substrates was carried out in air using a Multimode AFM equipped with a Nanoscope III controller (Veeco Instruments). The AFM was operated in tapping mode using single crystal silicon tips with nominal radius of curvature 5-10 nm and cantilever resonance frequency in the range 200-300 kHz. Scan areas were $2\mu\text{m} \times 1\mu\text{m}$ with scan rates of 1.5-2 Hz for each sample. Sampling resolution was 2048 x 512. Typically at least three images have been acquired on each sample. AFM images were processed using custom routines written in MATLAB[®] environment ¹. Each AFM-image was flattened subtracting a global plane and line-by-line first-or occasionally second-polynomial functions in order to get rid of the tilt of the sample and of the scanner bow. Root-mean-squared (σ) roughness, parameter which describe the surface morphology, has been calculated from:

$$\sigma = \sqrt{\frac{1}{N} \sum_{i,j} (h_{ij} - \bar{h})^2} \quad (3.1)$$

where h_{ij} represents the height values and N the number of height values in the AFM topographic map, \bar{h} is the average height. Root-mean-squared roughness is a measure of surface corrugation, i.e. of the dispersion of surface height values around the average height \bar{h} . The evolution of the surface morphology with

¹Matlab- version 7.4.0.287 (R2007a) The MathWorks Inc.

3.4 Nanostructured Zirconia Characterization

increasing annealing temperature was also investigated; in particular for five different degree steps from ambient temperature to 800°C. Samples were thermally annealed in air using an oven at 250-400-600-800°C, reached through a slow ramp and maintained for 2 hours.

3.4.2 X-ray Powder Diffraction

X-ray diffraction is a method used in the characterisation of the structures of crystalline materials which allows the identification of phases present and the determination of a given material's unit cell dimensions. By performing studies as a function of time, temperature, pressure or dynamic chemical environment it is possible to obtain information which will help the understanding of the behaviour of a material. When a material is exposed to an incident beam of X-rays, the X-rays interact with the atoms present which act as secondary point sources and re-radiate the X-rays in all directions. If the atoms exist in a periodic array, the constructive and destructive interference phenomenon of diffraction occurs. This can be most simply described in terms of Bragg's law. It was shown by W. L. Bragg that every diffracted beam of X-rays can be regarded as a reflection from sets of parallel planes of lattice points. The angles of incidence and reflection must be equal and co-planar with each other, whilst also being normal to the reflecting plane. To define a plane, three integers are required to detail its orientation with respect to the edges of a given unit cell. These are known as the hkl or Miller indices. The spacing between successive planes within a material is determined by the lattice geometry and thus d_{hkl} is a function of the unit cell parameters. The path difference, $2l$, between two reflected beams is equal to $2d\sin\theta$ (Figure

3. MATERIALS AND METHODS

3.5). If constructive interference is to occur this path difference must be equal to an integer number of wavelengths, $n\lambda$. This leads to the Bragg Equation 3.2.

$$2d\sin\theta = n\lambda \quad (3.2)$$

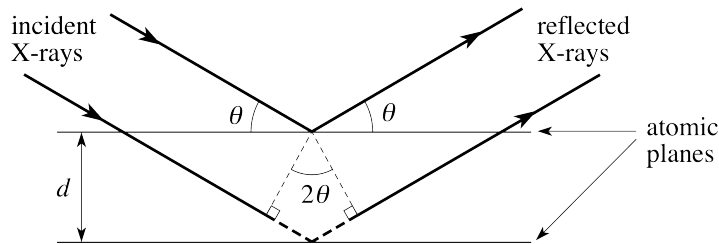


Figure 3.5: Diagram showing the path difference for two beams at angle θ reflected by different planes -

In a powder diffraction experiment, a large (ideally infinite) number of crystallites are placed in the path of an incident X-ray beam. Each crystallite in the powder sample gives rise to a discrete diffracted beam of X-rays. However, as there are an infinite number of randomly oriented crystallites, each individual diffracted beam becomes a cone (figure 3.6) of diffraction, and the individual hkl spots are distorted into rings of intensity. For a crystalline sample each set of lattice planes in a given material will be in every possible orientation, meaning at least one of each set of planes will be at the Bragg angle to the incident beam, thus leading to diffraction for those planes. When recording a powder diffraction pattern, we are therefore left with a one dimensional diffraction pattern expressed (typically graphically) as the diffracted intensity versus the diffraction angle, 2θ .

In order to quantify the changes in structure and microstructure of the material with temperature, Rietveld refinement can be performed on the data. Rietveld

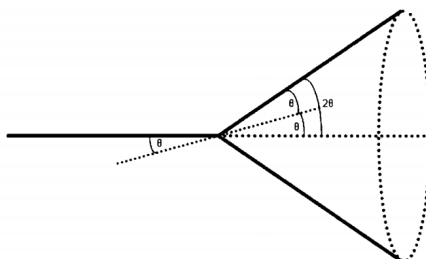


Figure 3.6: Diagram describing the formation of cones of diffraction when performing powder diffraction - X-rays travel from the source to the sample, at which point they are diffracted

analysis is a whole profile structure refinement method based on least-squares fitting. The powder diffraction pattern of the sample is obtained in digital form, and the Rietveld process treats these digital data as an intensity measurement (y_i) at each of several thousand increments (step -i). A calculated profile of the structure is compared to the experimental profile, and then selected parameters are refined by a least-squares method in order to provide the best fit between the calculated and experimental profiles.

3.4.2.1 Experimental

XRPD measurements have been performed at Elettra synchrotron radiation facility in Trieste, at the Material Characterization by X-ray diffraction beamline (MCX) in order to determine the thermal expansion and structure evolution, up to 1000°C, of nano-structured ZrO_{2-x} . To carry out the experiment it has been used a monochromatic radiation ($\lambda=0.7866\text{\AA}$) and the set up described in (65, 66). The powdered samples were obtained by scratching a pristine deposited

3. MATERIALS AND METHODS

film and then introduced in a quartz capillary inserted into a closed furnace, (see Figure 3.7) (for accurate temperature control in the range 25-1000°C) and sealed to a device able to switch from vacuum to air or inert gas (N₂) atmospheres.

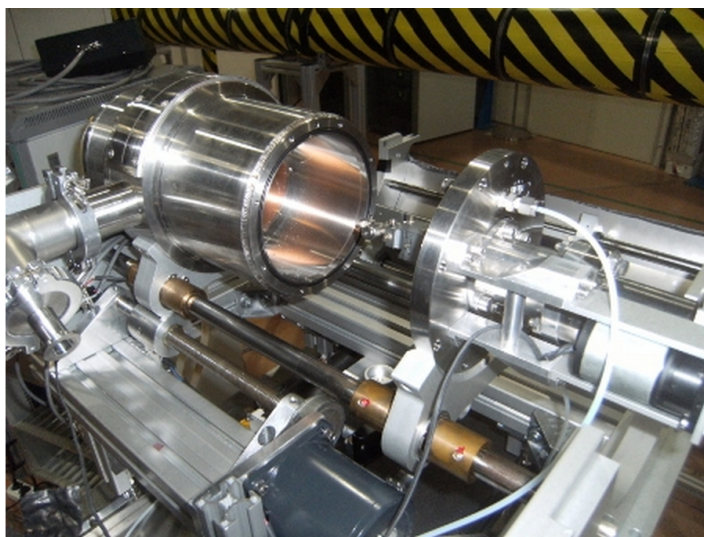


Figure 3.7: The MCX beamline endstation - Detail of the furnace implemented into the MCX beamline: the furnace provides an atmosphere and temperature controlled environment for powders in capillaries and a temperature controlled environment for thin-film samples.

Diffraction signals have been collected by translating curved (cylindrical) imaging plate detector to assure a constant sample-detector distance and avoid geometrical corrections for intensity. Raw data (pixel vs intensity) extracted with Fit2D software (67, 68) are converted into an angle/intensity histogram by a preliminary calibration performed with the NIST standard Si powder. Rietveld analysis of converted spectra has been performed with GSAS software (69). The accurate crystallite sizes have been calculated by fitting the whole XRPD spectrum. The

3.4 Nanostructured Zirconia Characterization

samples were undergone to thermal annealing in air and in moderate vacuum. The annealing treatments followed the same protocol for all the applied experimental measurements, namely a ramp of 50°C in 5 min and then heating the sample at fixed temperature for 20 min, In order to make comparable as much as possible the data obtained from different experimental techniques. For XRPD measurements the diffraction patterns were acquired with the sample held at fixed temperature inside a furnace mounted at the end of the beamline filled with air or evacuated at 10^{-3} mbar.

3.4.3 Electron Photoemission Spectroscopy

Photoemission spectroscopy (PS) is the most important and widely used experimental technique to gain information about occupied electronic states. This technique, extremely surface sensitivity, typically sampling the top 50-100Å of the material, direct consequence of the short mean free path (5-20 Å) of the low energy electrons through the sample, is based on the photoelectric effect (see Figure 3.8): when a solid is irradiated by light, photons excite electrons from occupied states into empty states (Within the solid), whence, if their energy exceed the solid work function, they are released into the vacuum and detected by an electron-energy analyzer.

The absorption of an incident photon of energy $h\nu$ causes the emission of an electron having energy:

$$E_{kin} = h\nu - E_i - \phi$$

where ϕ is the work function, the E_i , the binding energy of the electronic level

3. MATERIALS AND METHODS

excited by absorption of the photon, is a fingerprint of the different atomic species and also reflect their chemical environment. The use of synchrotron radiation to perform PS has the advantages of being high intensity, tunable with sharply defined photon energy, thus permitting selection of photon energy and to maximize the cross section for a transition of interest. Another advantages of PS is that the energy resolution of practical system is high enough to resolve the small changes in electron binding energy that accompany changes in the chemical state of the atom being excited.

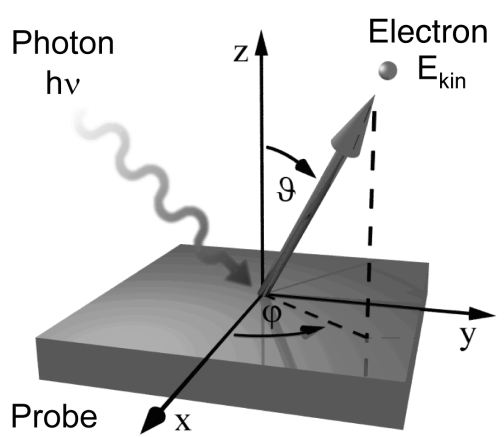


Figure 3.8: Sketch of Photoelectric effect -

These shifts arise from the fact that as electronic charge is added to or removed from a given atom in the process of forming chemical bond. The resulting change in the screening of the core electrons results in small changes in the energy of the allowed electronic states. The magnitude of these changes is on the order of 1 to 5 eV.

3.4 Nanostructured Zirconia Characterization

3.4.3.1 Experimental

The Photoemission experiments have been carried out at Materials Science Beamline (MSB) at the ELETTRA synchrotron radiation source in Trieste, Italy. The photoelectron spectra have been recorded at normal emission by a Specs Phoibos MCD 150 hemispherical analyzer operating for high resolution spectra at a pass energy of 20 eV. A gold mesh was used to measure the incoming photon flux. The photoemission spectra were acquired by using a photon energy of 650 eV or 320 eV and 50 eV with a photon energy step of 0.1 eV. The samples investigated are shown in Table 3.1.

Sample	Thickness	Roughness	Annealing	Gas exposition
SMP1	300 nm	30 nm	no	no
SMP2	300 nm	30 nm	150°C UHV	H ₂ O
SMP3	300 nm	30 nm	150°C UHV	CH ₃ COOH

Table 3.1: Samples tested - Overview of samples and measurements.

The samples have been mounted on special holder as shown in Figure 3.9 a, which allows the current passage for the sample heating and then inserted into the measurements chamber (Figure 3.9 b). The temperature has been measured by a Nichel-Chromium thermocouple till. The H₂O exposure has been performed for 20 minutes at 5×10^{-8} mbar (~ 45 L) while the CH₃COOH exposure for 6 minutes at 5×10^{-8} mbar (~ 15 L).

The error associated at the temperature measurements is around 10°C, enough for the scope of our experiments. Every measured photoemission line has been

3. MATERIALS AND METHODS

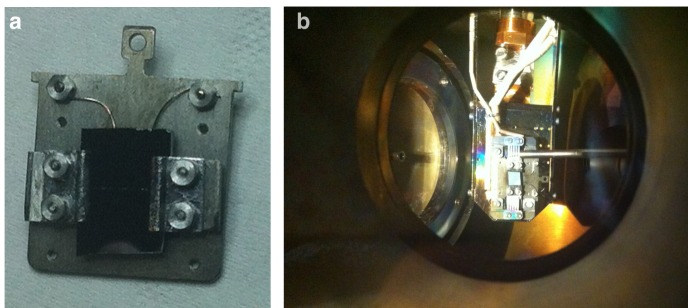


Figure 3.9: MSB endstation - In figure a the holder for the sample annealing by joule heating, in figure b the sample mounted into the chamber for XPS measurements

normalized dividing by the flux of incident photons to be comparable with the other lines, of the same electronic level, acquired at different time points.

3.4.4 High Resolution Transmission Electron Microscopy

HRTEM is a technique that uses the interaction of energetic electrons with the sample and provides morphological, compositional and crystallographic information. The electron emitted from filament passes through the multiple electromagnetic lenses and make contact with the screen where the electrons are converted into light and an image is obtained. The speed of electrons is directly related with the electron wavelength and determines the image resolution. A modern HRTEM is composed of an illumination system, condenser lens system, an objective lens system, magnification system, and the data recording system. A set of condenser lenses focuses the beam on the sample and an objective lens collects all the electrons after interacting with the sample and form an image of the sample, and determines the limit of image resolution. Finally, a set of intermediate

3.5 Customized aptamer microarrays

lenses magnifies this image and projects it on a phosphorous screen or a charge coupled device (CCD). HRTEM is an instrument for high-magnification studies of nanomaterials. High resolution makes it perfect for imaging materials on the atomic scale. A main advantage of a TEM over other microscopes is that it can simultaneously give informations in real space (in the imaging mode) and reciprocal space (in the diffraction mode). The high-resolution transmission electron microscopy (HRTEM) uses both the transmitted and the scattered beams to create an interference image. It is a phase contrast image and can be as small as the unit cell of crystal. All electrons emerging from the specimen are combined at a point in the image plane.

3.4.4.1 Experimental

The high resolution transmission electron microscopy experiments have been performed at the University of Cambridge using a FEI Tecnai F20 microscope operated a 200kV.

3.5 Customized aptamer microarrays

In order to find the right conditions for aptamer immobilization on cluster-assembled ZrO_2 the protocol developed by our group called Protein Surface Interaction Microarray (PSIM) for the hightroughput study of biomolecules-surfaces interaction (57, 70) has been used. The protocol consists in spotting small volume droplets of fluorescent biomolecules on the surface under investigation. After incubation, blocking, washing and drying, the amount of adsorbed biomolecules is

3. MATERIALS AND METHODS

evaluated by reading the fluorescent signal with a commercial microarray scanner, see figure 3.10.

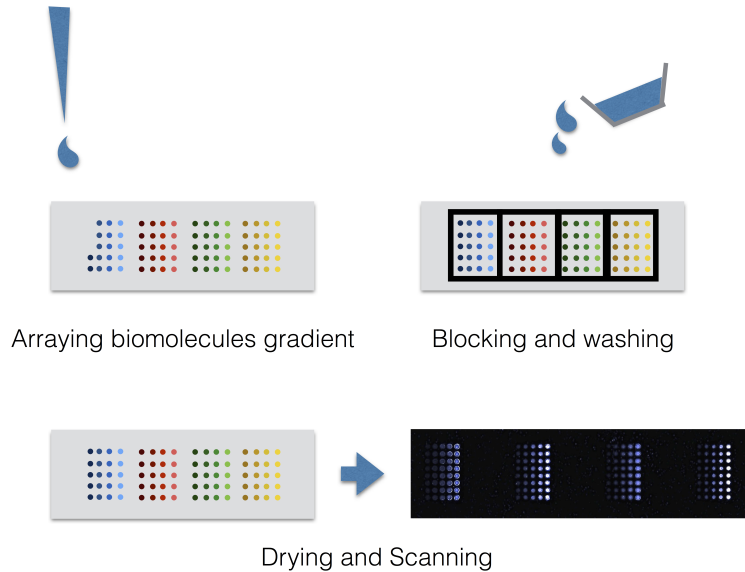


Figure 3.10: PSIM protocol - Sketch PSIM protocol: first fluorescent biomolecules solutions, in a wide range of dilution are spotted on several biomaterials in parallel. Secondly biomaterials slides are incubated in a controlled atmosphere, then immersed in a blocking solution and next rinsed. Finally, the slides are dried with a gentle nitrogen flux and the fluorescent signal is read with a commercial microarray scanner

3.5.1 Aptamers

The aptamers, SA20 and SA23, have been chosen among a panel of ssDNA described by Cao *et al.* in their work (53), to test the feasibility of the substrate as platform for biosensing application, moreover the aptamer SA17, described in (52), has been chosen after preliminary results indicating that the aptamer previously picked, in particular SA23, was not as specific as reported in the Cao's

3.5 Customized aptamer microarrays

paper. HPLC purified aptamers were supplied as lyophilized samples and then dissolved in PBS 1X buffer. SA20 and SA23 have been purchased from SIGMA-ALDRICH®, SA17 and SA23b Biotin-TEG modified have been purchased from PrimmBiotech. The aptamers are listed in the Table 3.2.

Aptamer	Sequence	mer	Labeling	Modification
SA20	GCAATGGTACGGTACTTCC	88	Cy5	none
	GCGCCCTCTCACGTGGCACTCAGA			
	GTGCCGGAAGTTCTGCGTTAT			
SA23	CAAAAGTGCACGCTACTTTGCTAA	88	Cy5	none
	GCAATGGTACGGTACTTCC			
	GGGCTGGCCAGATCAGACCCCGGA			
SA17	TGATCATCCTTGTGAGAACCA	62	Cy3	Biotin-TEG
	CAAAAGTGCACGCTACTTTGCTAA			
	TCCCTACGGCGCTAACCCCCCAGTCCGT			
SA23b	CCTCCCAGCCTCACACCGCCACCGTGCTACAC	88	Cy 3	Biotin-TEG
	GCAATGGTACGGTACTTCC			
	GGGCTGGCCAGATCAGACCCCGGA			
	TGATCATCCTTGTGAGAACCA			
	CAAAAGTGCACGCTACTTTGCTAA			

Table 3.2: Aptamers tested - Sequences, size, labelling, modification.

3.5.2 Immobilization of aptamers on nano-structured ZrO₂

In this study small droplets (450 pL) of fluorescent aptamers, indicated in table 3.2, dissolved in PBS buffer (pH 7.4) have been spotted at different concentrations, on cluster-assembled ZrO₂ using an automated sciFLEXARRAYER S3-Scienion AG spotter, Figure 3.11, in an array format at 65% controlled humidity

3. MATERIALS AND METHODS

in order to avoid drop evaporation. After spotting, slides have been incubated for 20 minutes at room temperature and 65% humidity. After incubation slides have been blocked once in BSA 2% (W/V) for 5 minutes and washed 3 times in PBS for 3 minutes and 3 times in doubly-distilled H₂O for 1 minute. Slides have been then dried under gentle nitrogen flux. Fluorescence was then quantified using a microarray scanner TECAN and images have been analyzed using Scan-array Express Software.

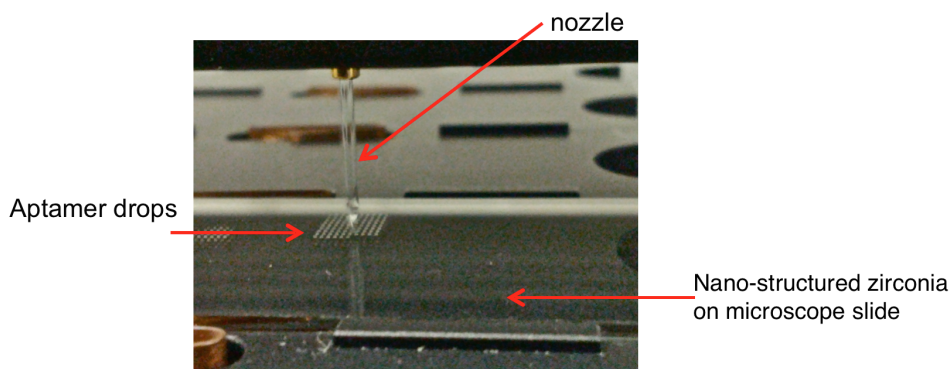


Figure 3.11: Microarray generation - In figure a step of the PSIM protocol: spotting of aptamers

A second protocol was followed after the preliminary results: the spotting conditions are the same but, after incubation, slides have been blocked once in blocking solution with PBSMT (PBS 1X + 5 mM MgCl₂+ 0.1% (V/V) Tween20) for 10 minutes and washed 3 times in PBSMT for 3 minutes, 3 times in PBSM (PBS 1X + 5 mM MgCl₂) for 3 minutes and finally in doubly-distilled H₂O for 1 minute. Slides have been then dried under gentle nitrogen flux. Fluorescence was then quantified using a microarray scanner TECAN and images have been analyzed using Scanarray Express Software.

3.5 Customized aptamer microarrays

3.5.2.1 Nano-structured ZrO₂ surface functionalization

In order to immobilize biotin-TEG 5'-functionalized aptamers, on the nanostructured surface via biotin-streptavidin binding, the zirconia surface was covered with streptavidin. In particular, a custom microarray was realized, with the technique described in Section 3.4, made only by 3 μ M Alexa 647 labeled streptavidin spots. This microarray was then used as substrate for the immobilization of biotin-TEG functionalized aptamers.

3.5.3 Test of immobilized aptamer activity

In order to verify if the aptamer immobilization conditions were suitable for the generation of a platform for bacterial detection a test to check the activity of the immobilized aptamers was conducted. In particular, a fluorescent peptide, conveniently designed by the Molecular Modelling Laboratory (Department of Chemistry, University of Parma), specific for SA23 aptamer, was used as probe. The testing procedure was conducted using aptamers microarray, as described in the Subsection 3.4.2, with an intermediate step of aptamers incubation with IIa.2 fluorescent peptide immediately after the blocking step. In particular, for the 15 minute incubation, a concentration of 20 μ M of fluorescein-labeled IIa.2 dissolved in PBS, was used. Then the fluorescence signal was imaged in the xy and xz planes using a Leica TCS SP5 confocal microscope, 20X dry objective, with 512 x 512 image resolution.

3. MATERIALS AND METHODS

3.6 Detection of *S. aureus*-aptamer interaction

To verify if the condition for immobilizing aptamers on nano-structured surfaces were right for the maintenance of aptamer activity and specificity for bacterial recognition, a direct test of bacteria detection was performed. Specifically the protocol presented here was followed:

- Incubation with 5 μ M streptavidin for 20 minutes
- Washing with PBSM, 1 time for 5 minutes
- Incubation with 5 μ M biotin-TEG-aptamer-Cy3 labeled for 15 minutes
- Washing with PBSMT, 3 times for 3 minutes
- Incubation with *S. aureus* or *E. coli*, 10⁸ bacteria/ml for 45 minutes at RT
- Washing with PBSMT and PBSM, 3 times for 3 minutes each
- Mount the slide with glycerol for confocal imaging

The bacteria were cultured in solution, using LB Broth (Miller) from SIGMA-ALDRICH[®] as growth medium, in a thermoshaker at 37°C overnight. Then the concentration of bacteria was measured using a spectrophotometer with fixed lambda ($\lambda=600$ nm). Before the incubation with immobilized aptamers the bacteria had been stained with Hoechst 33258 from SIGMA-ALDRICH[®] (3 μ l per ml of solution).

3.6 Detection of *S. aureus*-aptamer interaction

3.6.1 Fluorescence confocal microscopy

The microscope slides, prepared as described in section 3.4, had been imaged in the xy and xz planes using a Leica TCS SP5 confocal microscope using a Diode (561 nm) laser with 30% laser power, a 40X oil immersion objective, 1024 x 1024 image resolution and UV (405 nm) at 35% laser power, 40X oil immersion objective and 1024 x 1024 image resolution.

3.6.2 Electrophoretic Mobility Shift Assay (EMSA)

To assess the possible interaction between aptamers and the surface proteins of *S. aureus*, aptamers SA23 (53) and SA17 (52) have been tested with membrane proteins from Staphylococci cells. To this purpose, surface-associated proteins were prepared by lysostaphin treatment under isotonic conditions, as described (71). The detection of *S. aureus*-aptamer complexes was achieved by staining of the aptamers with SyBr Green, a cyanine dye capable of binding DNA with high affinity. In addition, *E. coli* was used as a negative control to ensure specificity of *S. aureus*-aptamer interactions. A detailed protocol follows:

Sample preparation

- *S. aureus* membrane protein extracts (SAUQC, SAU1, SAU2, SAU3) after lysostaphin treatment: 50 μg
- *E. coli* extracts (negative control): 50 μg
- Aptamers SA23/SA17: 5.5 μg , 11.8 μg

3. MATERIALS AND METHODS

- Binding buffer: 0.5 M Tris-HCl pH 6.8, 10% (V/V) glycerol for 30 min at 25°C

Electrophoretic Mobility Shift in native conditions

- Non denaturing polyacrylamide gel at 4%, 6%, 8%, 10%, 12% concentration
- Electrophoresis buffer: Tris/Borate/EDTA (TBE) 0.25X, 20 mM, pH 7,5
- Pre-run: 20 min at 100 Volt constant
- Run: 140-210 Volt constant for 2 hrs at 4°C

Detection and acquisition of band

- DNA sequence
 - SyBr Green I
 - Chemidoc and Quantity-one
- Protein extracts
 - Silver acid/Silver basic/Blue Comassie
 - GS-800 and Quantity-One

4

Results and Discussion

In this chapter, the results obtained in this work will be presented. In the first section, the growth and characterization of cluster-assembled zirconia, which will be subsequently used as platform for aptamer immobilization, are presented. Morphological characterization of cluster-assembled ZrO_{2-x} thin films reveals a correlation between the film thickness and its surface roughness and an evolution of the surface roughness as a consequence of high temperature annealing. Moreover the crystalline structure and the spectroscopic characteristics of these cluster-assembled thin films have been investigated respectively by XRPD, HRTEM and PS. In Section 4.2, the protocol followed for the aptamer immobilization on cluster-assembled ZrO_{2-x} thin films and the surface functionalization are described. In section 4.3, the preliminary results about bacteria-immobilized aptamer interaction are discussed.

4. RESULTS AND DISCUSSION

4.1 Nanostructured Zirconia

By the use of the SCBD, cluster-assembled thin films, deposited on glass microscope slides and silicon substrates, have been realized (as described in Section 3.1). For the investigation of the role of temperature in the morphology evolution, samples with thickness ranging from 50 nm to 600 nm have been analyzed. For the XRPD study a sample obtained by scratching the material deposited on glass was investigated. For the PS study a sample with a thickness of 300nm characterized by a roughness of 30 nm was examined. For the immobilization of aptamers two kinds of cluster-assembled thin films, deposited on glass microscope slides in many replicates, have been realized: one type with a thickness of 70 nm and one type with a thickness of 300 nm. For the HRTEM measurements the samples have been deposited on glass substrates and then scratched in order to get a powder which was placed on a TEM grid coated with Carbon.

4.1.1 Morphological Characterization

Since the surface roughness is crucial in the molecules immobilization affecting the adsorbed density of molecules and their functionality (57, 58), AFM characterizations have been performed. The overall film morphology of cluster-assembled zirconium oxide thin films is characterized by nanometer-scale porosity and granularity, dominated by grains of size 5-20 nm, which represent the aggregates of primeval zirconium clusters produced in the cluster source. It is possible to see how the roughness increases as the thickness of the material deposited increases (Figure 4.1 A-D). AFM topographic images show an uniform evolution in the

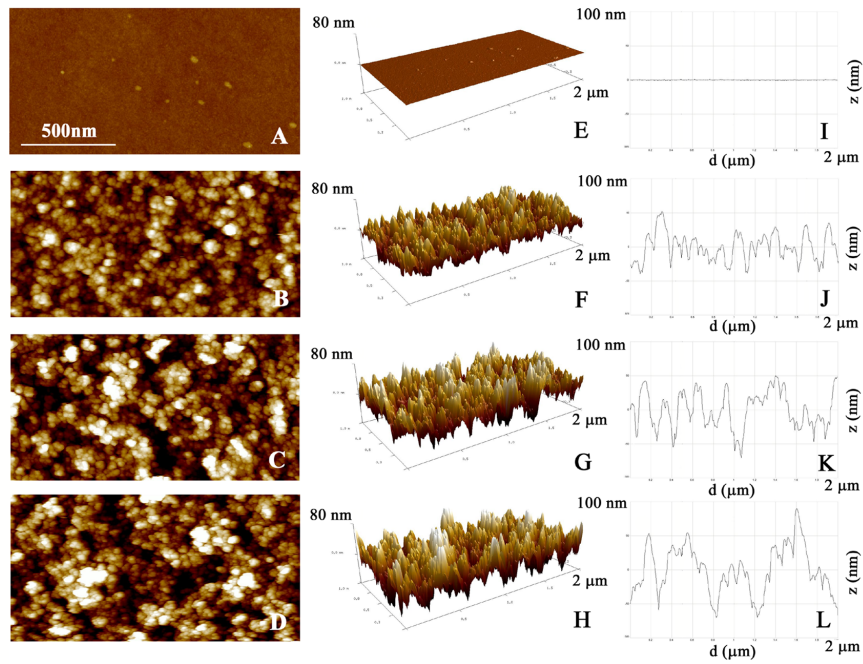


Figure 4.1: AFM analysis of nanostructured zirconium oxide surfaces with increasing level of roughness - B-D AFM topographic images showing uniform evolution in the surface morphology with increasing film thickness to different levels of nanoroughness as evident from surface scan profiles I-L. A Surface topography of flat zirconium reference and **I** cross section profiles shows flat substrate characteristics. Three-dimensional visualization of AFM topography **E-H**. All images corresponds to $2 \times 1 \mu\text{m}^2$ scan area. Note that **A,E,I**: smooth zirconium; **B,F,J**: 50 nm; **C,G,K**: 100 nm, **D,H,L**: 200 nm thick ns-ZrO_x film.

4. RESULTS AND DISCUSSION

surface morphology with increasing film thickness to different level of nanoroughness as evident from surface scan profile in Figure 4.1, **I-L**.

The cluster-assembled ZrO_{2-x} behaviour under heating conditions was also investigated in order to understand better the evolution of surface morphology in view of a possible way to control the morphology just by thermal treatment. The evolution of surface morphology depending on the effect of thermal annealing of five samples with thickness ranging from 50 nm to 600 nm was studied in more detail. In figure 4.2 the topographic maps of the sample 150 nm thick, after different thermal treatments (as indicated by the labels) are shown.

In figure 4.2 by comparing each single image, it is possible to notice that the surface maintains its nanostructure nature also after thermal annealing treatments at high temperature. Although the nanostructured is preserved, the surface roughness has a small increase after thermal treatment, as shown in Figure 4.3. This roughness enhancement can be explained by the growth of grain size after coalescence promoted by the temperature or by the phase transition as shown by XRPD analysis (see Section 4.1.2). The evolution of grain dimension in cluster-assembled zirconium oxide thin films is still under investigation.

Since from the AFM results we have seen that temperature plays a fundamental role for the roughness evolution and grain size growth, we characterized the influence of temperature on crystalline structure of the thin films by Fast Fourier Transform (FFT) analyses of HRTEM images and XRPD measurements. Moreover, as performed for the AFM measurements, we investigated the role of temperature in crystalline phase transition.

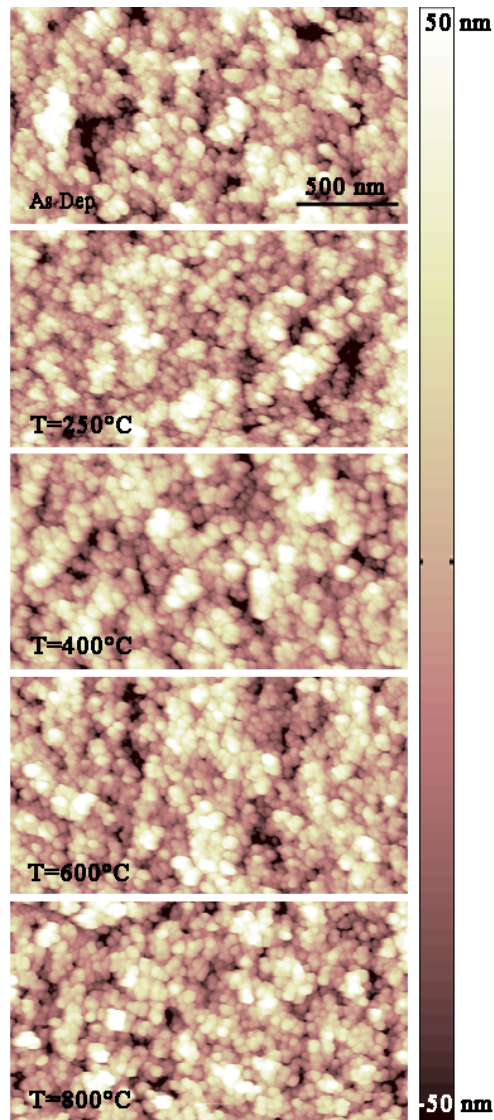


Figure 4.2: ns-ZrO_{2-x} surface topographic maps - Surface morphology evolution of a sample characterized by a thickness of 150nm depending on thermal annealing process, from as deposited sample, at 250°C, 400°C, 600°C and 800°C

4. RESULTS AND DISCUSSION

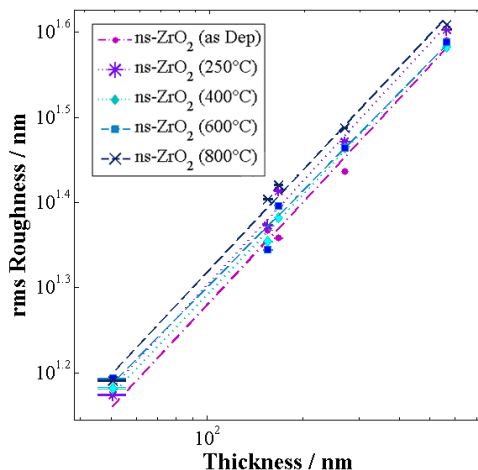


Figure 4.3: Evolution of roughness vs thickness - In the graph are shown the trend of roughness increasing after thermal treatment at 250°C, 400°C, 600°C and 800°C

Figure 4.4 **a** represents a TEM micrograph of a pristine sample, whereas figure 4.4 **b** is a sample after annealing up to 950°C in air. The size of the nanoparticles composing a thin film, characterized by a roughness of 18 nm before and after annealing in air up to 950°C, was extrapolated from TEM images. The grain size histograms in figure 4.5 confirm that the annealing treatment promotes the increase of the grain size of the cluster-assembled zirconia films. In particular the nanocrystal diameter dispersions, for the sample annealed at 950°C is more than doubled with respect to the non-annealed sample (see Figure 4.5 **b**). Moreover, the mean value of the particle size increases from 6 nm, for the non-annealed sample, to 14 nm, for the thermal-treated sample, demonstrating how the temperature fosters grain coalescence.

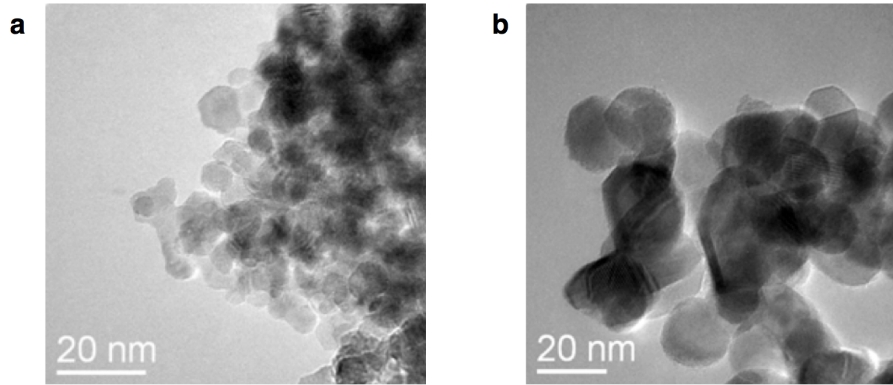


Figure 4.4: TEM images of cluster-assembled zirconia oxide films before and after annealing - In panel **a** the image of a deposited cluster-assembled zirconia; in **b** the image of cluster-assembled zirconia annealed up to 950°C in air.

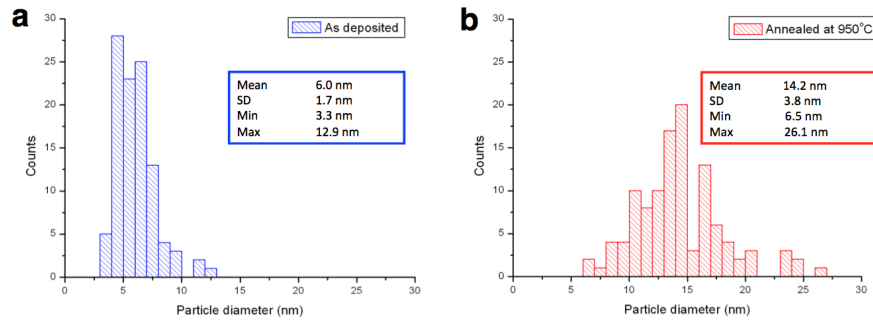


Figure 4.5: Hystograms of grain diameters distributions for a cluster-assembled zirconia films before and after annealing - In **a** nanoparticle diameter distribution extrapolated from the TEM image for the sample not annealed; in **b** nanoparticle diameter distribution extrapolated from the TEM image for the annealed sample up to 950°C in air

4. RESULTS AND DISCUSSION

4.1.2 Structural Characterization

To characterize the structure of the material, before and after thermal treatment, a Fast Fourier Transform analysis of HRTEM images was performed. The FFT of the lattice related to the non-annealed sample matches a cubic phase pattern, as shown in Figure 4.6, whereas the FFT of the lattice corresponding to the annealed sample matches the monoclinic phase pattern as shown in Figure 4.7.

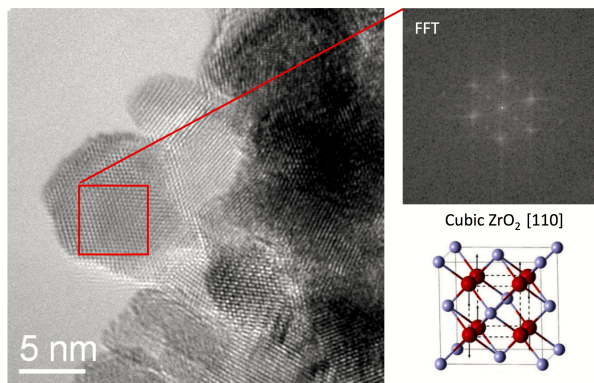


Figure 4.6: FFT of cluster-assembled zirconia films not annealed - Zoom of HRTEM image of nanoparticles forming the non-annealed sample; in the top right is the FFT of the image; in the bottom right is the theoretical model of the cubic crystal phase.

From this structural analysis it is evident that cluster assembled films are formed by the aggregation of small nanocrystals having the highest structural symmetry and that the annealing process, in air, induces grain size increasing (confirming the AFM results) together with phase transition. The x-ray powder diffraction (XRPD) pattern for the pristine sample is shown in Figure 4.8. Within the limit of the experimental resolution, the structural Rietveld fit is compatible with zirconia

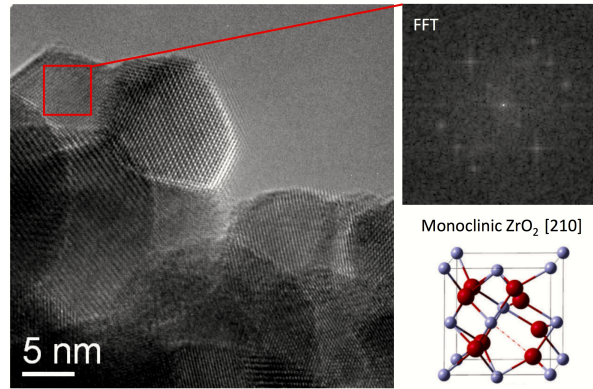


Figure 4.7: FFT of cluster-assembled zirconia films annealed at 500°C - Zoom of HRTEM image of nanoparticles forming the sample annealed at 500°C; in the top right is the FFT of the image; in the bottom right is the theoretical model of the monoclinic crystal phase

in cubic phase with a refined unit cell parameter of 5.1253(5) Å. The annealing experiments were performed either in air and in low vacuum ($\sim 10^{-3}$ mbar), in order to assess the role of the oxygen abundance in the phase transition and in the change of nanocrystal size.

The increasing of temperature is then expected (as detected by FFT analysis of HRTEM images) to favor the transition from the metastable cubic phase to the stable monoclinic phase in the range of temperatures examined (see section 3.4.2.1), but even the amount of the available molecular oxygen can foster the phase transition by promoting the full oxidation of the sample. With these experiments we want to investigate how the mutual occurrence of thermal energy and oxidizing environment leads to the coalescence of adjoining nanocrystallites. Figure 4.9 reports the fractions of the cubic and monoclinic phases as a function

4. RESULTS AND DISCUSSION

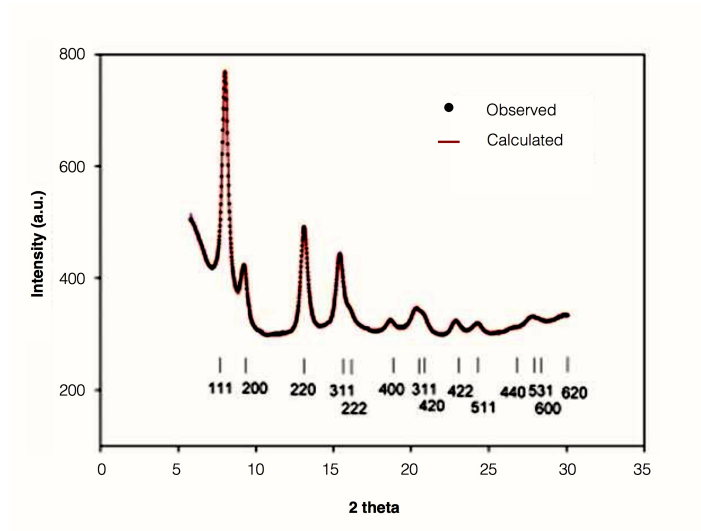


Figure 4.8: Diffraction graph of cluster-assembled zirconia showing X-ray intensity as a function of 2-theta angle - The peak positions indicate the cubic crystal phase of the non-annealed sample.

of the annealing temperature. The top panel shows the behavior in vacuum, whereas the bottom one in air. As the temperature increases, the plots reveal the appearance of the monoclinic phase and the decreasing of the cubic phase. The generation of the stable phase takes place at 190°C and 480°C in air and in vacuum respectively. The transition from cubic to monoclinic structures is activated at lower temperature in air rather than in vacuum. Indeed the intersection of the fractions of cubic and monoclinic phases at 50% occurs at 647°C in vacuum and 477°C in air, even though the phase transition is completed (all of the components are characterized by a monoclinic phase) at the same temperature. The observed different rapidity indicates that once the transformation is primed the temperature is the main ruler of the process. However, it is interesting to observe as the same thermal treatment is operated in air and in low vacuum the

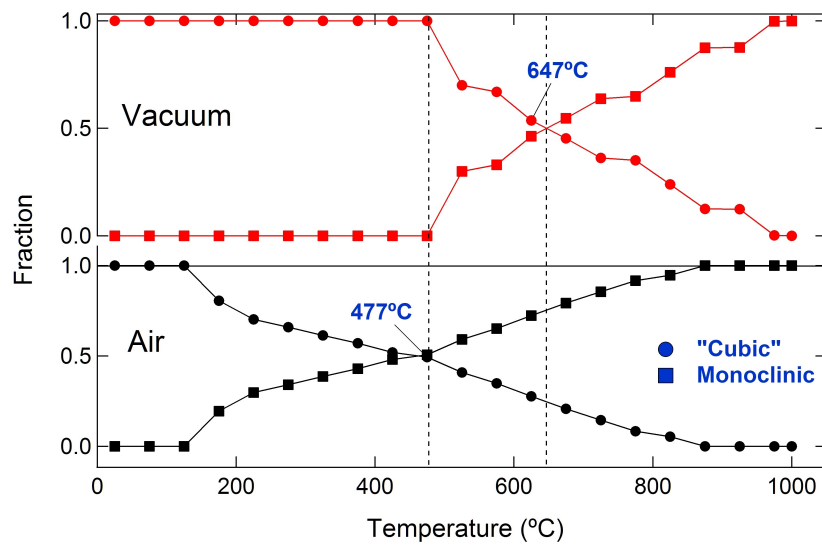


Figure 4.9: Plot of the fraction of monoclinic and cubic crystal phase in function of temperature - The graph shows the trend followed by the fraction of crystal phases of cluster-assembled zirconia films during the annealing in air (bottom graph) and in vacuum (top graph). In air the transition starts before that under vacuum conditions, and the 50 % fraction of cubic and monoclinic occurs at 647 °C in vacuum and 477 °C in air. In both cases a complete shift from cubic to monoclinic phase is reached around ~ 850 °C

4. RESULTS AND DISCUSSION

trigger of the phase transformation is not only due by the temperature but also by the abundance of oxygen. Thus, even if the data are related to the followed heating-up protocol, it can be argued that the oxygen has a fundamental role in the phase change as well as in the aggregation of the nanocrystals. Investigating the growth of the nanocrystal dimension of the cubic and monoclinic phases as a function of the annealing temperature, we see in Figure 4.10 that in the the pristine sample the dimension of the crystallites is around 5 nm, in good agreement with the mean value obtained with the analysis of the grain size distribution from TEM images (6.0 ± 1.7 nm). From figure 4.10 it can be also observed as the annealing in a more oxidizing environment favours nanocrystal growth, almost doubling diameter in size (~ 75 nm) at about 1000 °C with respect to the vacuum case (~ 40 nm). From these results, in agreement with AFM and HRTEM measurments, we can speculate that oxygen has a relevant role in promoting and favouring crystal coalescence and phase transition although is closely related to the temperature.

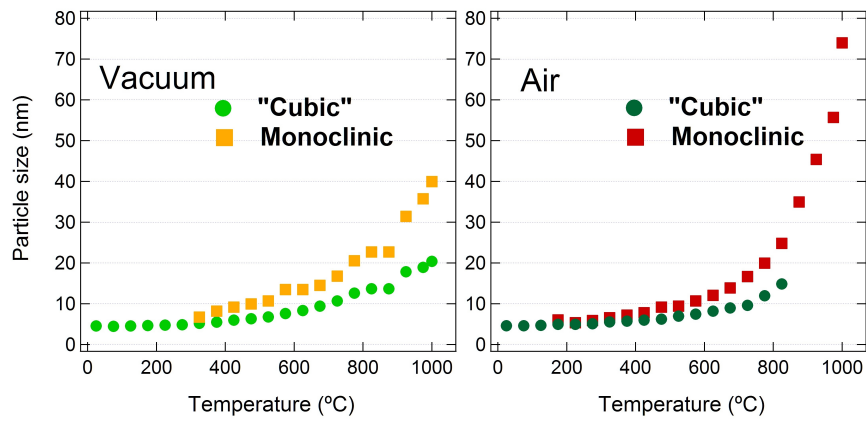


Figure 4.10: Plot of particles size dimension versus temperature - In the plot on the left is shown the trend followed by nanoparticle size dimensions as a function of temperatures for both the cubic and monoclinic phases of cluster-assembled zirconia films annealed in air. The plot on the right shows the trend followed by nanoparticle size dimensions as a function of temperatures for both the cubic and monoclinic phases of cluster-assembled zirconia films annealed in vacuum. It is evident how the vacuum conditions favour the growth of the nanoparticles size. In particular, the dimensions of grains for the sample annealed in vacuum reach ~ 75 nm while the dimensions of grains for the sample annealed in air reach ~ 40 nm

4. RESULTS AND DISCUSSION

4.1.3 Spectroscopic Characterization

Interfaces between metal oxide and biologically active molecules are important in biocatalysis, biocompatibility and biosensors. For this reason we investigated the reactivity of the cluster-assembled ZrO_{2-x} towards water and acetic acid (used as model of carboxyl-terminated compounds such as aspartic acids and glutamic acids which are amino acid residues of streptavidin), characterizing by photoemission spectroscopy (PS) the C_{1s} , O_{1s} , Zr_{3d} core levels and the valence-band of the sample listed in Table 3.1. To promote the desorption of atmospheric contaminants from the surface, films have been fairly annealed *in situ* (1×10^{-9} mbar) at 150°C for 15 minutes. C_{1s} peak was used as reference for the binding energy scale (C_{1s} binding energy for carbon contamination is fixed at 285 eV). The spectra analyzed have been normalized according to the I_0 and Shirley-type background was subtracted. In Figure 4.11 the Zr_{3d} core level spectra of the samples described in table 3.1: two contributions corresponding to the $\text{Zr}_{3d_{5/2}}$ and $\text{Zr}_{3d_{3/2}}$ are recognizable. In particular, for the sample as deposited, they are situated at 182.0 eV and 184.3 eV, respectively. For the sample exposed to water for 20 minutes at a pressure of 5×10^{-8} mbar the peaks are shifted 0.5 eV, towards higher energy, with respect to the peaks corresponding to the as deposited sample. The peaks belonging to the sample exposed to acetic acid for 6 minutes at a pressure of 5×10^{-8} mbar are shifted 0.3 eV, towards higher energy, with respect to the peaks corresponding to the as deposited sample. To notice how the effect of the exposition to molecules containing oxygen pushes the maximum of the peaks, characteristics of Zr_{3d} core level spectra, in the direction of high energy; which

is evidence of the increasing degree of oxidation of the cluster-assembled zirconia surface.

In Figure 4.12 the C_{1s} XPS core-level spectra are shown. Four contributions characterize this spectra: one at 285.0 eV is representative of C-C and CH bonds, one at 285.8 eV is peculiar to the C-OR bond (where R stays for residues e.g., hydrogen (H)), one at 287.2 eV distinctive of C=O bond and the last one at 288.9 eV characteristic of O=C-OR bond. It is interesting to notice the shift of the peak corresponding to the O=C-OR bond after water and acetic acid exposure towards higher energy. Moreover the intensity of the peak corresponding to O=C-OR bond of the sample exposed to acetic acid increases as a consequence of the adsorption of the carboxyl group by the porous surface of cluster-assembled zirconia. The intensity of the O=C-OR peak for the sample exposed to water it is not increased too much, with respect to the intensity of the peak of the sample exposed to acetic acid, even if it has been exposed to a higher concentration. The reason behind this behaviour can be the lower affinity of cluster-assembled zirconia for water compared to acetic acid.

In Figure 4.13 the O_{1s} XPS peak of the 3 cluster-assembled zirconia films samples consisting of a component at 530.1 eV corresponding to O-Zr bond, another component at 531.9 eV corresponding to O-R bonds and the last one at 532.3 eV representative of O=C-R bond.

The as deposited sample presents a shoulder distinctive of the combined effect of atmospheric contamination and O-R bond, which disappears in the spectra of the sample exposed to water, this effect is mainly due to the effect of the annealing at 150°C which removed the contamination. For the sample exposed to acetic

4. RESULTS AND DISCUSSION

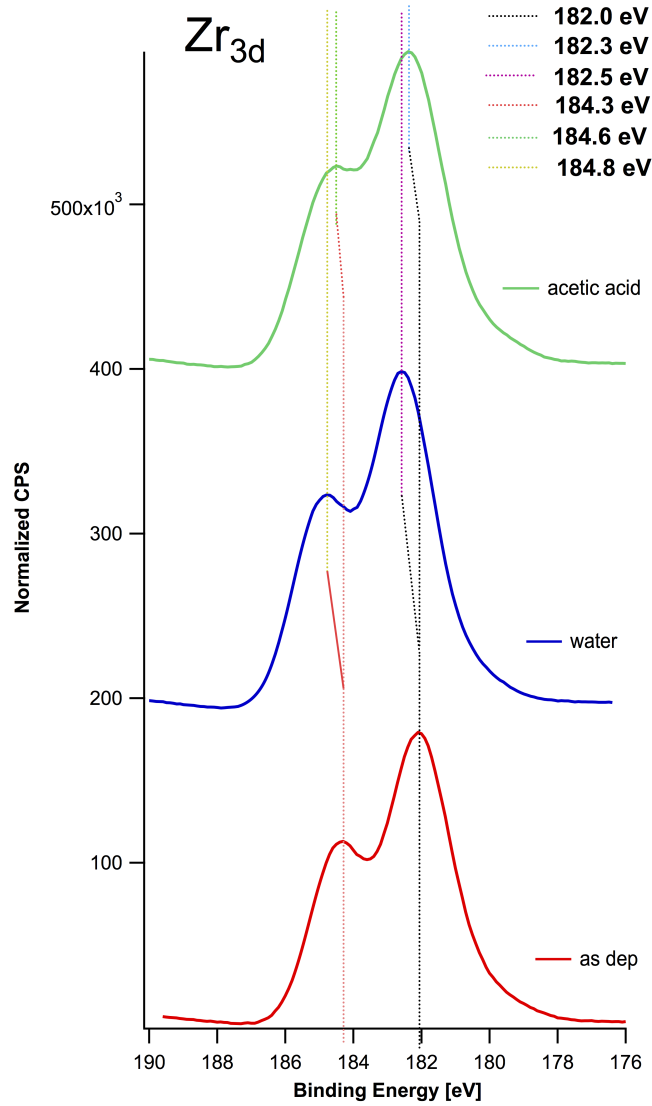


Figure 4.11: Zr_{3d} core level spectra - On the bottom, in red, the spectra of the as deposited sample, in the middle, in blue, the sample exposed to 45L of water: the peak corresponding to the Zr_{3d_{5/2}} level is shifted 0.5 eV from the same peak into the as deposited sample, on the top, in green, sample exposed to 15L of acetic acid: also in this case the peak corresponding to the Zr_{3d_{5/2}} is shifted 0.3 eV

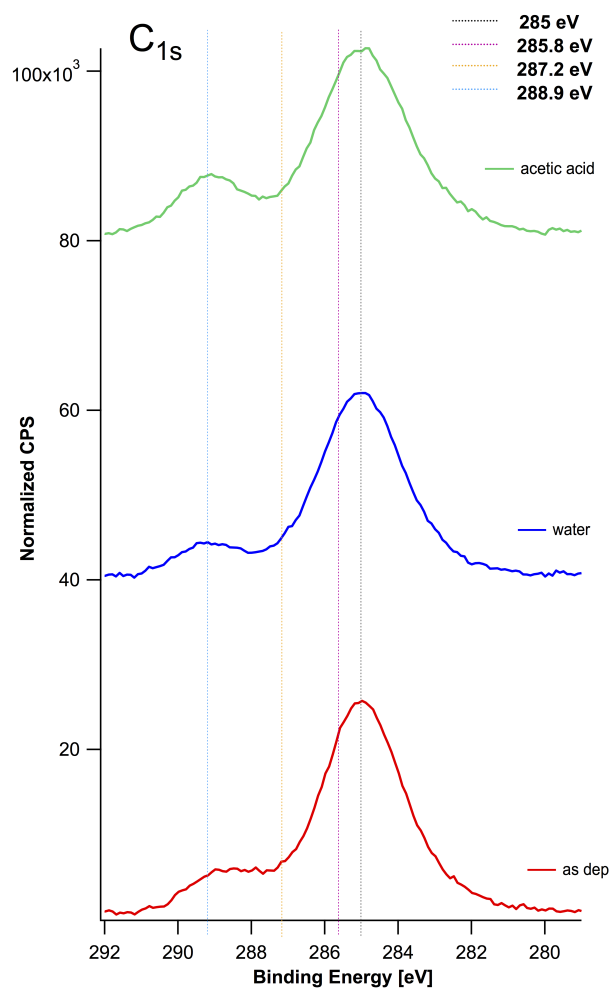


Figure 4.12: C_{1s} core level spectra - On the bottom, in red, the spectra of the as deposited sample, in the middle, in blue, the sample exposed to 45L of water, on the top, in green, sample exposed to 15L of acetic acid

4. RESULTS AND DISCUSSION

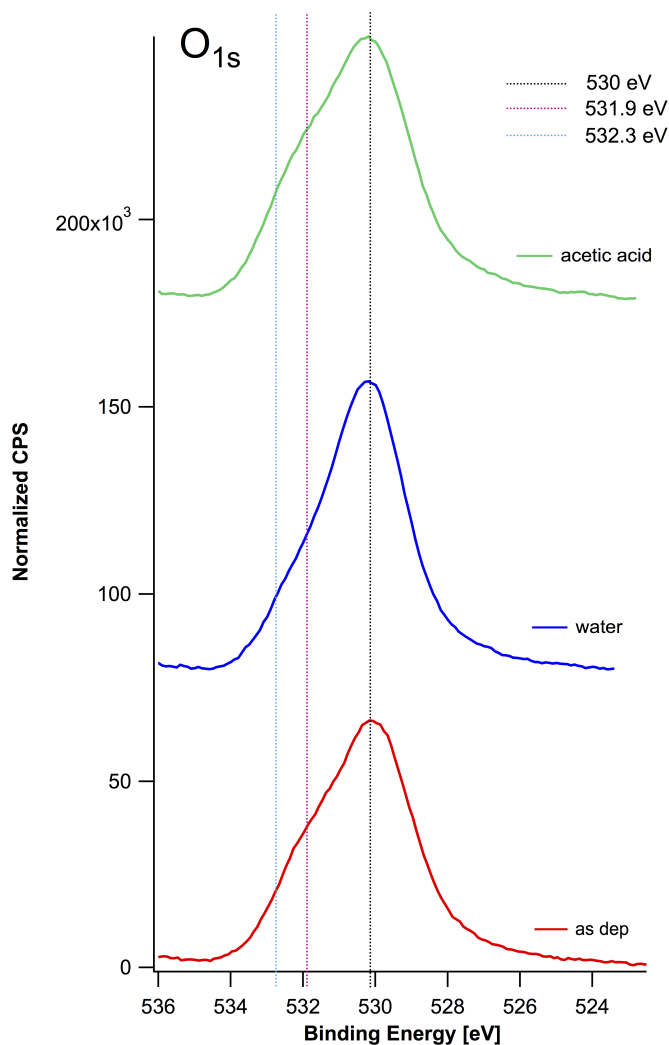


Figure 4.13: O_{1s} core level spectra - On the bottom, in red, the spectra of the as deposited sample characterized by a shoulder at 531.9 eV representative of O-R bond, in the middle, in blue, sample exposed to 45L of water: the shoulder at 531.9 eV is not present anymore, consequence of the annealing treatment, on the top, in green, the sample exposed to 15L of acetic acid: the shoulder at 532.3 eV is characteristic of O=C-OR bond

acid, this shoulder is slightly moved to 532.3 eV and more pronounced respect to the as deposited sample. Although this sample has undergone an annealing the shoulder is still present meaning that the COOH group of the acetic acid reacted with the surface of cluster-assembled zirconium oxide.

In figure 4.14 the UPS spectra of VB of four samples, three samples as described in table 3.1, and one sample just annealed at 150°C for 15 minutes: VB states in the range of 5-12 eV are related to O_{2p} orbitals with some admixing of Zr valence states (72, 73). The features, below the VB, at 15.5 eV can be attributed to residual atmospheric contamination, the peak at 23.7 eV corresponds to O_{2s} orbital while the peak at 33 eV is due to Zr_{4p} .

In figure 4.15 a comparison between the VB of the as deposited sample and the sample exposed to water molecules is shown and, at the bottom of the graph is also reported the difference between the spectra. In particular it is possible to notice the rising of the signal of hydroxyl groups coming from dissociative water adsorption (3σ states of OH^- placed at about 11 eV) and the broadening of the O_{2s} signal.

The VB states for the as deposited sample show two peaks, which are a bit more defined with respect to the samples exposed to water and acetic acid. This difference can be explained by the increase in oxygen and carbon species adsorbed on the cluster-assembled zirconia surface. In figure 4.16 a comparison between the VB of the as deposited samples and the sample exposed to acetic acid molecules, at the bottom of the graph it is reported the difference between the two spectra. Also in this case the signal increases close by 11 eV and 28 eV. The VB states start to lose the two peaks shape respect to the as deposited sample.

4. RESULTS AND DISCUSSION

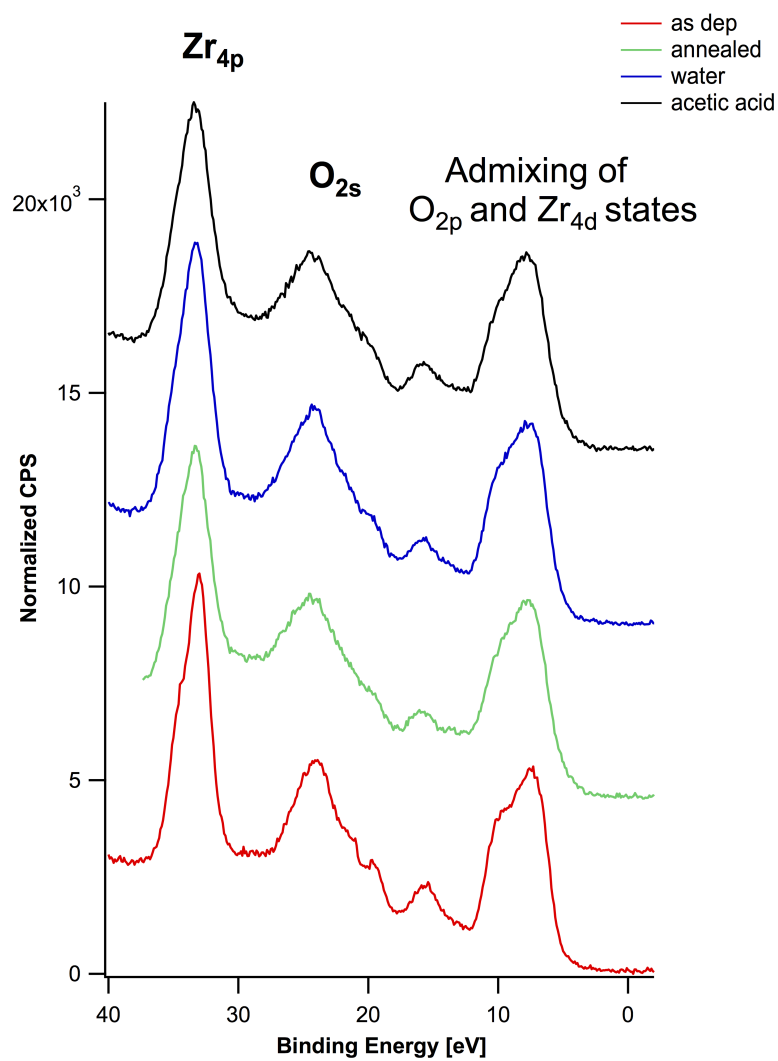


Figure 4.14: VB spectra of cluster-assembled zirconia - From the bottom to the top: the VB of the as deposited sample; VB of sample annealed at 150°C in UHV; VB of sample exposed to 45L of water and VB of sample exposed to 15L of acetic acid.

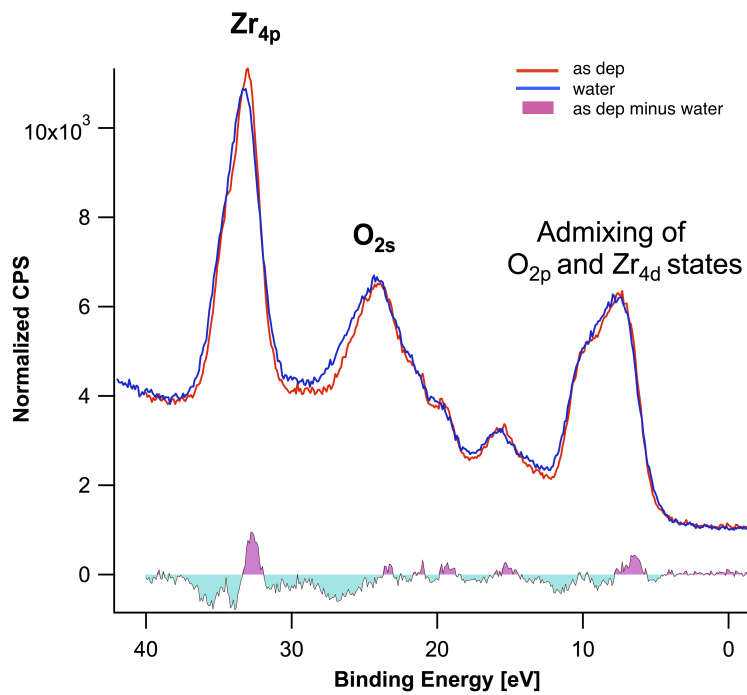


Figure 4.15: VB spectra of the as deposited and water exposed cluster-assembled zirconia films - The graph shows the two UPS spectra of the sample before and after water exposure. In the bottom the signal coming from the difference between the VB of the as deposited sample and the VB of the sample exposed to 45L of water. Main differences are in the 10-13 eV and 23-33 eV ranges.

4. RESULTS AND DISCUSSION

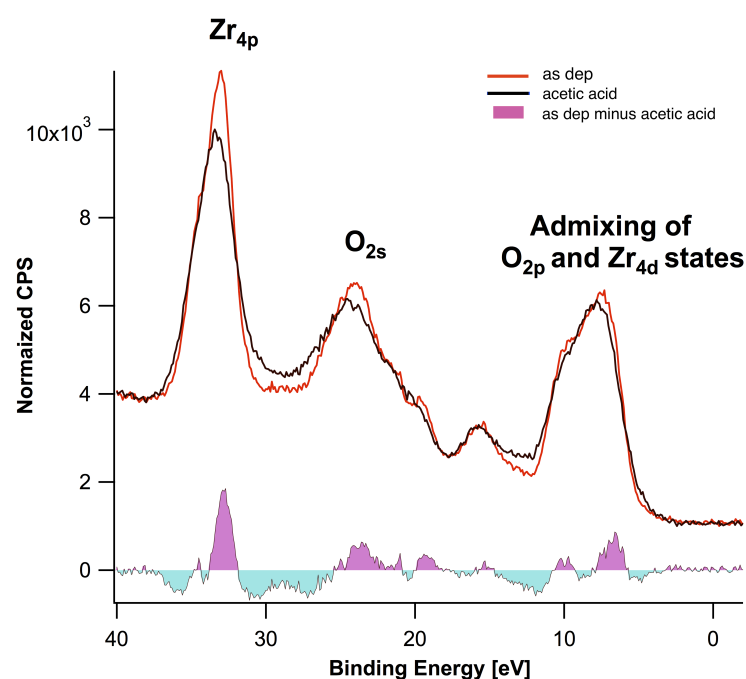


Figure 4.16: VB spectra of the as deposited and acetic acid exposed cluster-assembled zirconia films - The graph shows the two UPS spectra of the sample before and after acetic acid exposure. In the bottom the signal coming from the difference between the VB of the as deposited sample and the VB of the sample exposed to 45L of water. Main differences are in the 10-13 eV and 23-33 eV ranges

4.2 Aptamer-functionalized nanostructured Zirconia

Comparing figures 4.15 and 4.16 the difference between the two spectra in the range of 10-13 eV and 23-33 eV, is more pronounced for the sample exposed to 15L of acetic acid. Since the amount of molecules facing the zirconia surface is less in the case of acetic acid exposure but the signal is higher with respect to the water exposure we can imagine that the cluster-assembled zirconia surface is more reactive towards molecules exposing COOH groups.

4.2 Aptamer-functionalized nanostructured Zirconia

In order to exploit the possibility to realize an aptamer-based biosensor for bacteria detection it has been taken advantage of the microarray technique in order to test different experimental conditions for aptamers immobilization in one single experiment. Moreover, these microarrays have been used to test bacteria-aptamer interactions. In figure 4.17 is shown the layout of the aptamer-microarray created to test the bacteria-aptamer interaction.



Figure 4.17: Aptamer-microarray - Microscope slide coated with a thin film of nano-structured zirconia with spots of aptamers (described in table 3.2).

4. RESULTS AND DISCUSSION

From images acquired by the commercial scanner reader it is evident that the aptamers are immobilized on the nanostructured surface since we are seeing a fluorescence signal (figure 4.17). But this is not sufficient to assert that the aptamers are immobilized in a functional way allowing them to be "active" in bacterial recognition. So to verify that the immobilizing conditions applied in the micorarray generation were appropriate directly the aptamer-microarray with a labeled-peptide probe (section 3.5.3) designed *ad hoc* for aptamer SA23 was tested. We expected a fluorescence signal coming from the hybridization between SA23 and peptide IIa_2 and no signal from the others aptamers immobilized on the nanostructured zirconia surface. Actually what we found was no signal at all. It means that the aptamers once immobilized on nano-structured zirconia do not keep their functionality. It is likely that some interactions (such as electrostatic interaction between aptamers negatively charged phosphodiester backbone and the charge of the surface) occurs between aptamers and surface leading to incorrect folding of the aptamer. To overcome this problem it was decided to use modified aptamers with Biotin-TEG (74) increasing the oligo-biotin distance to 15 atoms using a triethyleneglycol (TEG) spacer, in order to avoid any possible interaction between surface and the aptamers. In this way the immobilization of the aptamer, on the previously coated streptavidin nano-structured zirconia, takes place through the well known biotin-streptavidin binding. The new microarray has been tested with the fluorescein-labeled peptide (IIa_2) and the result is shown in figure 4.18.

4.2 Aptamer-functionalized nanostructured Zirconia

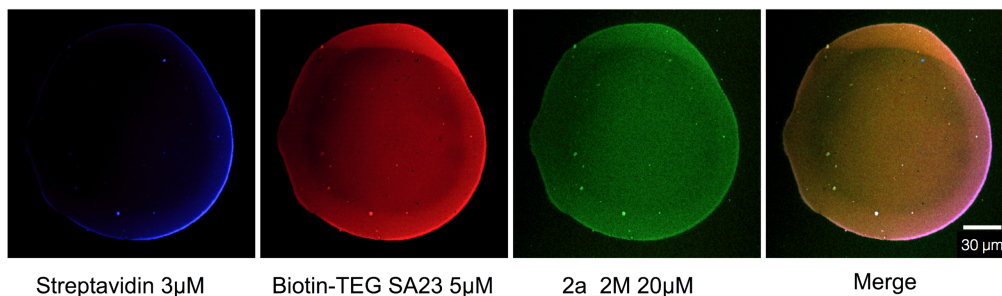


Figure 4.18: Confocal microscopy: XY view spots on ns-ZrO₂ - From left to right spot of streptavidin physisorbed on cluster-assembled zirconia surface, SA23 aptamer functionalized with Biotin-TEG immobilized on the surface via Biotin-Streptavidin bindings, peptide used as probe for the SA23 aptamer, merge of the three fluorescence signals

In this case the expected signal coming from the hybridization between SA23 and IIa_2 is visible in figure 4.18. It tells us that the aptamer has been immobilized keeping the correct folding. Images of the layers of biomolecules absorbed on the nano-structured zirconia surface have been acquired, as shown in figure 4.19.

4. RESULTS AND DISCUSSION

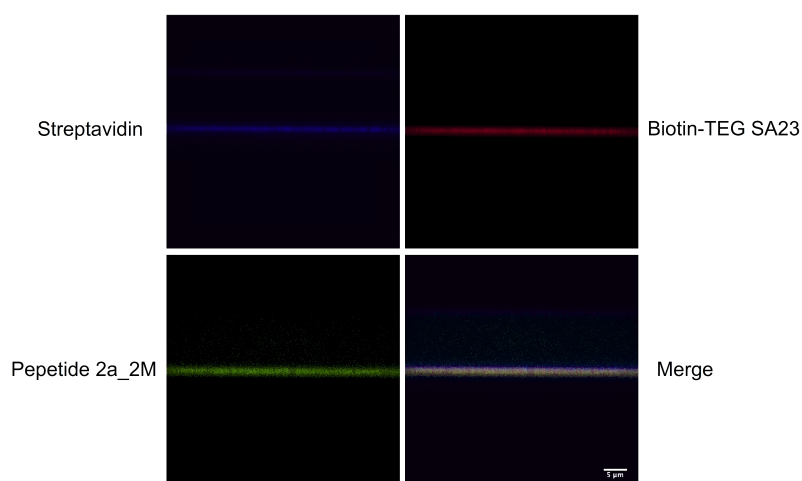


Figure 4.19: Confocal microscopy: Z view spots on ns_ZrO₂ - Layers of adsorbed fluorescent biomolecules on cluster-assembled zirconia surface. Clockwise from the top left: layer of 3 μM streptavidin, 5 μM SA23 aptamer, 20 μM peptide and the resultant merging of the three fluorescence signals.

4.3 *S. aureus*-aptamers interaction

Within the Cariplo's project it was decided to focus on the single aptamer SA23 (53) for the first proof of concept for the aptasensor realization. For this aptamer a specific peptide IIa.2 had been designed. Nevertheless I decided to test in parallel a recently published (52) aptamer specific for *S. aureus* since the preliminary results on SA23 specificity for *S. aureus* were not promising. Following the protocol described in section 3.4 and imaging the microarray by the use of a confocal microscope we have found no significant differences in *S. aureus* or *E. coli* recognition by the SA23 microarray, as it is possible to see in figure 4.20. From these results it would seem that the aptamer is not specific for the *S. aureus*. This finding is also confirmed by an EMSA experiments performed by the proteomics group, at Fondazione Filarete, led by Professor Gabriella Tedeschi (described afterwards).

4. RESULTS AND DISCUSSION

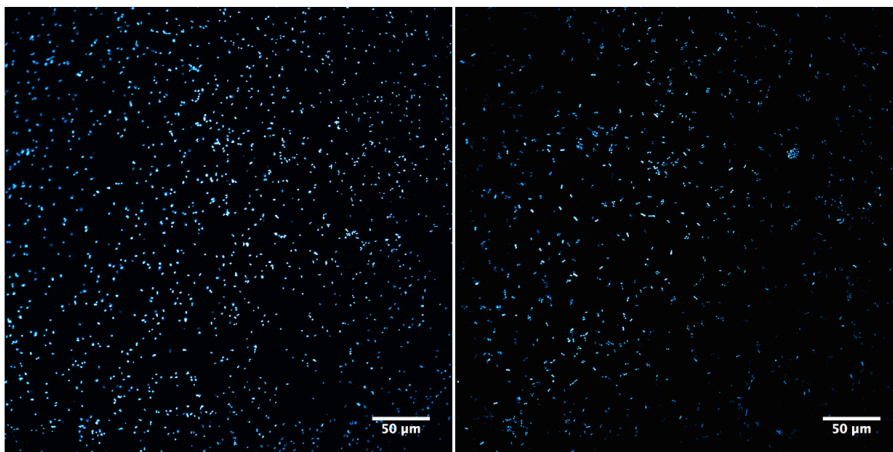


Figure 4.20: Confocal microscope images of Bacteria - On the left image *S. aureus*, stained with Hoechst, hybridized with previously immobilized SA23 aptamer; on the right *E. coli*, stained with Hoechst dye, hybridized with previously immobilized SA23 aptamer. Both bacteria have been incubated at a concentration of 10^8 bacteria/mL.

As stated before, in parallel an investigation was conducted on aptamer SA17 (52). In this case, although some *E. coli* bacteria have been found stuck on the aptamer-functionalized nanostructured zirconia, they are far less than *S. aureus* (see figure 4.21). Also for this aptamer an EMSA experiment was conducted which confirms the specificity of SA17 versus *S. aureus*. In figure 4.22 a particular along z axis of the bacteria "recognized" by the aptamer immobilized on nanostructured zirconia.

4.3 *S. aureus*-aptamers interaction

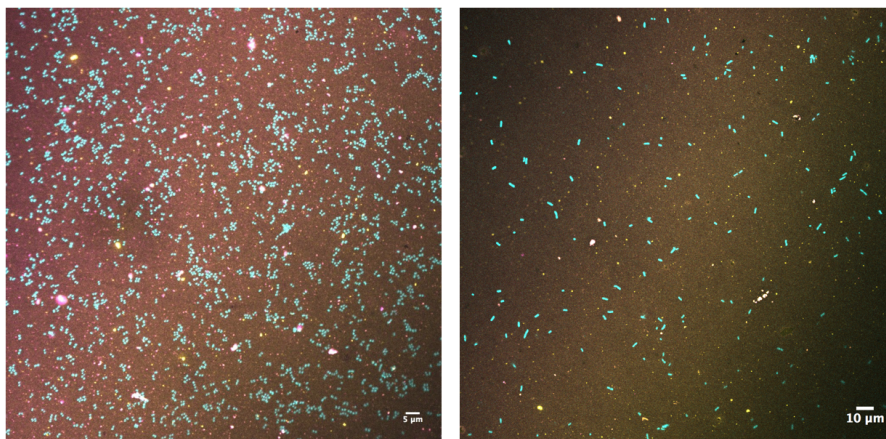


Figure 4.21: Confocal microscope images of Bacteria - On the left image *S. aureus*, stained with Hoechst, hybridized with previously immobilized SA17 aptamer; on the right *E. coli*, stained with Hoechst dye, hybridized with previously immobilized SA17 aptamer. Both bacteria have been incubated at a concentration of 10^8 bacteria/mL.

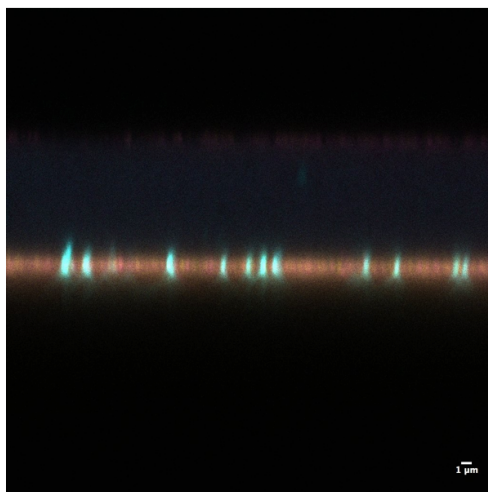


Figure 4.22: Confocal microscopy: Z-axis view of bacteria - Layers of adsorbed aptamers on nano-structured zirconia surface and *S. aureus* bacteria stuck on it

4. RESULTS AND DISCUSSION

Through EMSA experiments we tested the interaction between SA23-*S. aureus* with SA23-*E. coli* being used as a negative control. It is possible to see in figure 4.23 **a** and **b**, the regions highlighted in red into the lane corresponding to the complex aptamer-bacteria, in which it is possible to speculate the presence of interaction between aptamer-bacteria protein, are present also in the negative control *E. coli*.

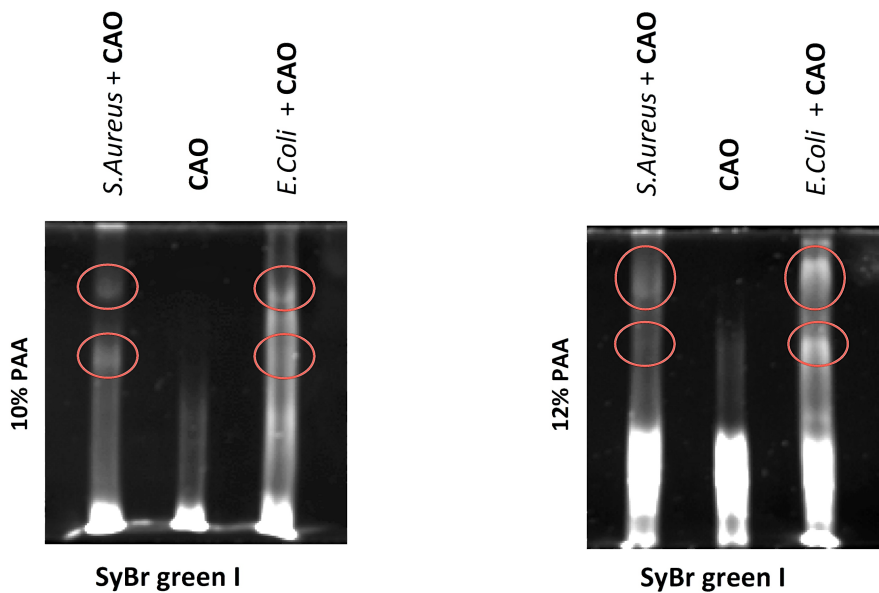


Figure 4.23: SA23 aptamer-Bacteria interaction - EMSA results at two different gel concentrations 10% and 12% PAA. In both figures, the two regions highlighted in red where it is possible to suppose interaction between aptamer-protein, are visible also in the negative control.

This result leads up to assert that interaction between SA23-*S. aureus* has non specific behaviour. For this reason we decided to discard the use of SA23 in the subsequent experiments addressed for the realization of an aptamer-based

4.3 *S. aureus*-aptamers interaction

biosensor for bacterial detection. A specific binding between aptamer SA17 (52) and *S. aureus* was observed particularly on native 10% polyacrylamide gels (figure 4.24).

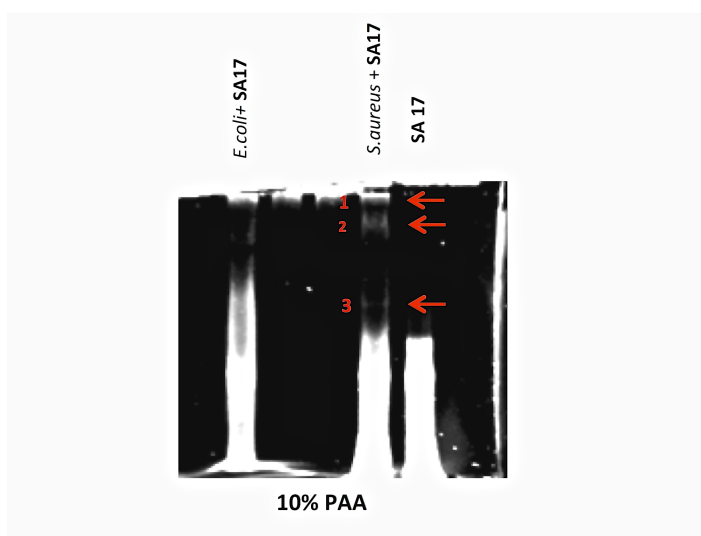


Figure 4.24: SA17 aptamer-Bacteria interaction - EMSA results of interaction between SA17 aptamer and *S. aureus*: three different regions of possible aptamer-protein interaction are visible (indicated by the arrows).

Therefore, the specificity of SA17 binding using three different clinical strains of bacterium (figure 4.25) was evaluated. Changing the strain of *S. aureus*, the same regions were identified on the gel, regions where we suppose there is an interaction between bacteria-protein. The result suggest that the proteins that bound to the aptamers are the same and are independent of the clinical strain under investigation. No evidence of interaction between SA17 aptamer and *E. coli* was found. All these results suggest that the aptamer SA17 is strain-specific. A step forward was made by identifying the proteins bound to the aptamer SA17 by tandem mass spectrometry. Bands, detected on Silver stained-gels, have been

4. RESULTS AND DISCUSSION

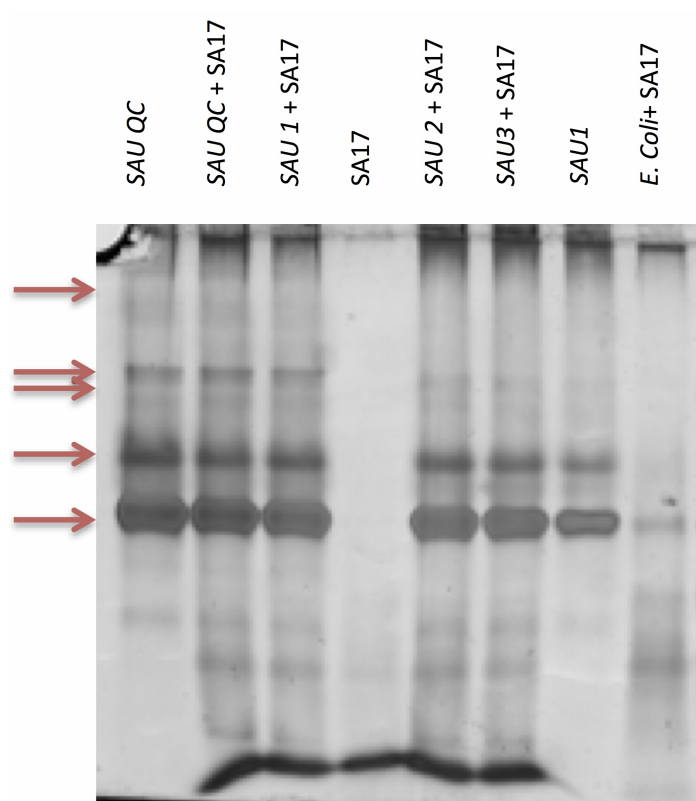


Figure 4.25: Comparative analysis of 3 different *S. aureus* strains - By changing the strain of *S. aureus*, on the gel, the regions where it was supposed there was an interaction between bacteria and protein are indicated by the arrows. No interaction found with *E. coli*.

4.3 *S. aureus*-aptamers interaction

excised and digested *in situ* by trypsin. Peptides have been separated by liquid chromatography using an ultimate 3000 HPLC and directly electro-sprayed into the LTQ-Orbitrap.veelos mass spectrometer. Data base searching was performed using the Sequest search engine contained in the Proteome Discoverer 1.1 software. Four proteins have been identified that share Gram positive cocci surface proteins LPxTG motif profile and NEAT domain:

1. serine aspartate repeat-containing protein E/sdrE
2. iron-regulated surface determinant protein A/IsdA
3. surface protein/SasE
4. immunoglobulin G binding protein A/spA

Only proteins identified in at least three different experiments have been considered as positively identified.

4.4 Summary

The zirconia nano-structured substrate developed in this PhD project is promising as platform for the generation of a biosensor based on the immobilization of receptors for the detection of biomolecules to pathogenic agents.

In particular, microarray technique opens to the possibility to develop biosensor able to screen in parallel more target since the chance to immobilize multiple receptors, on the same substrate, retaining their structure and functionality. Moreover the high surface-to-volume ratio that characterize the porous materials on which the microarrays are created, allows the adsorption of an higher amount of biomolecules in a functional way with respect to a flat surface (57, 58).

4.4.1 Development of a substrate for aptamer immobilization

Due to the SCBD technique we can control the roughness of the material we want to produce just by controlling the thickness of the material deposited. Moreover, it is important to highlight the fact that by changing the roughness we are not changing the surface chemistry properties. This makes the cluster-assembled zirconia films a material suitable for the investigation of the role of the nanoroughness, in biomolecules adsorption, cell growth and differentiation, without introducing other parameters. Cluster-assembled zirconia presents characteristics of thermal stability, in fact, as described in section 4.1.1, the surface maintains its nanostructured nature even after thermal annealing treatments at high temperatures. Another important quality of these zirconia nano-structured substrates is

the crystalline phase which characterize the as deposited thin films; in fact it is cubic with some content of tetragonal phase, as described in section 4.1.2, and it presents a transition to a monoclinic phase which is temperature and pressure-dependent. Since the crystal phase it is crucial for the bioactivity of zirconia thin films (75, 76), our investigation exploited an important parameter that we can control by post deposition treatment such as thermal annealing. Moreover, the investigation of Zr_{3d} , O_{1s} , C_{1s} core-level and valence band of sample exposed to water and acetic acid molecules revealed that the cluster-assembled zirconia surface is more reactive towards carboxyl groups rather than hydroxyl group.

4.4.2 Aptamer immobilization on zirconia nano-structured substrate

The cluster-assembled zirconia developed in this PhD work was used as a solid support for immobilization of bioactive molecules, in particular aptamers, for biosensing applications. The protocol developed for their immobilization preserves the functionality of the nucleotides, as discussed in section 4.2. In theory this substrate can be considered as an "universal" platform for biomolecular immobilization. What should be kept in mind is that some adjustments to the buffer solutions should be addressed, depending on the characteristics of the biomolecules under study. However, what can help in this sense is the possibility to combine the nanostructure with the microarray technique, providing the possibility to conduct experiments in an high-throughput way and test many conditions in only one test.

4. RESULTS AND DISCUSSION

4.4.3 Bacteria recognition *via* immobilized aptamer

The advantages of using aptamers as receptors for biomolecules, bacteria or other biological entities recognition was already discussed in the introduction. With this PhD work we attempted to demonstrate the feasibility to couple the aptamers with nanostructured materials in order to improve the sensitivity and selectivity of an aptamer-based biosensor, besides the possibility to develop a diagnostic tool for *S. aureus* which can be cheap, not time consuming, disposable and easy to use by anyone without particular skills. The preliminary results presented here, (see section 4.3), seem promising for the realization of an apta-sensor. Unfortunately the aptamer initially selected for the *S. aureus* recognition did not satisfy the requirement of specificity, although Cao et al. (53) reported this aptamer as specific for *S. aureus* within a panel of aptamers selected against *S. aureus* by Systematic evolution of ligands by exponential enrichment (SELEX), so it has not been possible to test the final goal of this project. Nevertheless another aptamer was selected, SA17 (52), and this seems to be promising for the achievement of the final goal of this project, even if more experiments need to be performed in order to improve the *S. aureus* binding *via* aptamers immobilized on the nanostructured zirconia and also to prevent the non-specific binding of *E. coli*.

4.5 Future perspectives

To achieve the final aim of the Cariplo's project a few more steps are still necessary. In particular it can be helpful to find more aptamers specific for *S. aureus* by performing new SELEX experiments, or finding new aptamers specific for the


4.5 Future perspectives

proteins, identified by tandem mass spectrometry in order to create a microarray with a panel of aptamers specific for *S. aureus*, thus improving the selectivity of the aptasensor. Moreover this approach can be used to develop an innovative biosensor (e.g. electrochemical, optical, electronic) where it is necessary to immobilize bioreceptors and retain their functionality. Furthermore, these substrates are suitable for cell culturing since they present good properties for cell adhesion, growth, maintenance and differentiation.

4. RESULTS AND DISCUSSION

5

Appendix



OPEN

SUBJECT AREAS:
FLUORESCENCE
IMAGING

IMAGING TECHNIQUES
SCANNING ELECTRON
MICROSCOPY

CONFOCAL MICROSCOPY

Received
23 July 2014

Accepted
23 October 2014

Published
13 November 2014

Correspondence and
requests for materials
should be addressed to
M.F. (maura.
francolini@
fondazionefilarete.
com; maura.
francolini@unimi.it)

* These authors
contributed equally to
this work.

Customized patterned substrates for highly versatile correlative light-scanning electron microscopy

Lorena Benedetti^{1,2*}, Elisa Sogne^{1,3,4*}, Simona Rodighiero¹, Davide Marchesi¹, Paolo Milani^{1,3} & Maura Francolini^{1,2}

¹Fondazione Filarete for Biosciences and Innovation, Viale Orles 22/4, 20139, Milan, Italy, ²Department of Medical Biotechnology and Translational Medicine, Università degli Studi di Milano, and National Research Council (CNR) Neuroscience Institute, Via Vanvitelli 32, 20129 Milan, Italy, ³Interdisciplinary Centre for Nanostructured Materials and Interfaces (CIMaINa), and Department of Physics, Università degli Studi di Milano, Via Celoria 16, 20133 Milano, Italy, ⁴European School of Molecular Medicine (SEMM), IFOM-IEO, Via Adamello 16, 20139 Milano, Italy.

Correlative light electron microscopy (CLEM) combines the advantages of light and electron microscopy, thus making it possible to follow dynamic events in living cells at nanometre resolution. Various CLEM approaches and devices have been developed, each of which has its own advantages and technical challenges. We here describe our customized patterned glass substrates, which improve the feasibility of correlative fluorescence/confocal and scanning electron microscopy.

The aim of correlative light electron microscopy (CLEM) is to combine the benefits of being able to observe the sub-cellular features of living cells by means of light microscopy (LM), and reveal their ultrastructural details using electron microscopy (EM)^{1–3}. The technique is challenging because it is necessary to switch from one device to the other: each requires an appropriately prepared sample, and one significant bottleneck is caused by the slow and laborious process of relocating a region of interest identified by light microscopy when switching to the electron microscope.

There are two principal types of CLEM: fluorescence/confocal microscopy with transmission electron microscopy (TEM) or scanning electron microscopy (SEM). The first has seen the development of various protocols and devices⁴, and is widely used in biological laboratories^{5,6}, but the second is still relatively undeveloped^{7–9}, and one of its prevailing limitations is the lack of substrates that are optimally suited for relocating the sample when switching from one imaging mode to the other³, in the absence of a single microscope equipped to do both^{8,10,11}.

In order to overcome this limitation, we have produced transparent, metal-patterned glass coverslips that are ideal for high-resolution confocal microscopy, allow cell growth and proliferation, are resistant to electron microscopy sample preparation procedures, and provide optimal contrast for SEM location. Commercially available etched substrates for optical microscopy have proved to be expensive and incapable of providing sufficient contrast for the SEM relocation of samples, whereas our patterned coverslips are cheap and rapid to produce, can be used with all optical and scanning electron microscopes, and are easily customized in terms of the choice of deposited metal and pattern design (Supplementary Figs. 1–3).

As proposed by Jimenez *et al.*,² we initially selected a square-based pattern for experiments using flattened HEK and HeLa epithelial cells (see Methods). Each basic element of the pattern consisted of six solid $150 \times 150 \mu\text{m}$ squares surrounding a letter, was precisely the same size as that of the field of view of the $20\times$ objective of the light microscope ($775 \times 775 \mu\text{m}$) in order to facilitate the rapid mapping of a number of regions of interest, and was repeated 25 times (5 rows \times 5 columns) so that it fitted the central area of a 10 mm round glass coverslip (Supplementary Figs. 1 and 2b).

A second, circle-based pattern was designed for experiments using cultured neurons, which are characterised by a cell body (soma) with a diameter of about $30 \mu\text{m}$ that has a number of protruding thin, branching neurites with a length of tens of micrometres. The correlative analysis of neuronal morphology and neurite branching requires a larger free coverslip surface in order to exclude any possible effect due to interactions between the cell structures and the deposited metal, and so the basic element consists of eight $70 \mu\text{m}$ diameter solid circles surrounding a letter or a number (Supplementary Figs. 1 and 2a), repeated 30 times (5 rows \times 6 columns). Its

SCIENTIFIC REPORTS | 4 : 7033 | DOI: 10.1038/srep07033

SCIENTIFIC REPORTS SREP-14-05275-T.3d 3/11/14 16:04:32

1



size was selected on the basis of the same criterion as that used to determine the size of the square-based basic element.

These two models fully satisfied our cell relocation needs, but the same technical approach can be used to customise the pattern on the basis of whatever cell shape (Fig. 1a).

We then used a stainless steel laser-cut mask to transfer the chosen template to normal cell culture coverslips by means of a conventional evaporation system based on the electron beam deposition (EBD) of the metallic target (Fig. 1b). In order to find the metal and film thickness that most easily identified the patterns using either microscopic technology, we tested gold, titanium and zirconium, all of which are known to be biocompatible and support cell adhesion and growth^{12,13}. The best results were obtained using 70 nm thick deposits of gold, 100 nm thick deposits of titanium, or 100–150 nm thick deposits of zirconium (Supplementary Fig. 3c), although all of the described experiments were performed using titanium because it is less expensive than the other metals, and the process of EBD is faster (see Methods). The patterned coverslips were sterilized and functionalized before seeding the cells, and cell viability and density proved to be completely unaffected by the presence of the metal deposits after 24–48 hours of culture (Supplementary Fig. 4). The adherent cells were transfected with vectors encoding for the proteins of interest and fluorescent tags, and the fluorescent signal in a subset

of living cells was acquired by means of low-magnification confocal microscopy using fields of view containing the pattern coordinates. After confocal imaging, the cells were fixed and processed for SEM (see Methods) and, by using the reference markers on the coverslips, we could immediately identify the same subset of cells, acquire higher-resolution SEM images, and analyse all of the acquired data (Fig. 1c).

This method was used to confirm the results of a previous study¹⁴ of the effects of the overexpression of protein 4.1R (a major structural element of the membrane cytoskeleton)¹⁵ in HEK cells. Confocal microscopy suggested that 4.1R overexpression led to a number of structural changes: the transfected cells were characterised by a larger surface area and greater filopodia protrusion, a phenotype that was completely reverted when ICln (a multifunctional cytosolic protein)¹⁶ was overexpressed together with 4.1R (Fig. 2a). The HEK cells were transfected with vectors containing the nucleotide sequence encoding for 4.1R or ICln, and a fluorescent protein (EGFP or DsRed) separated by an IRES sequence (see Methods), and the use of our square-based patterned coverslips allowed us to analyse the same fluorescent cells expressing 4.1R alone (Fig. 2b), ICln alone, or both 4.1R and ICln, which were first identified by means of confocal microscopy and then imaged using the scanning electron microscope (Fig. 2c). The magnification and resolution of the EM consistently

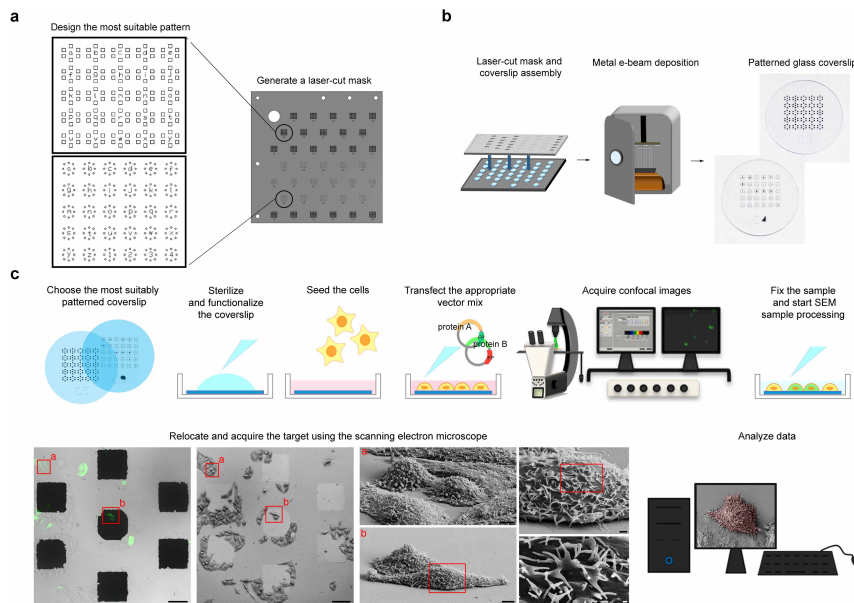
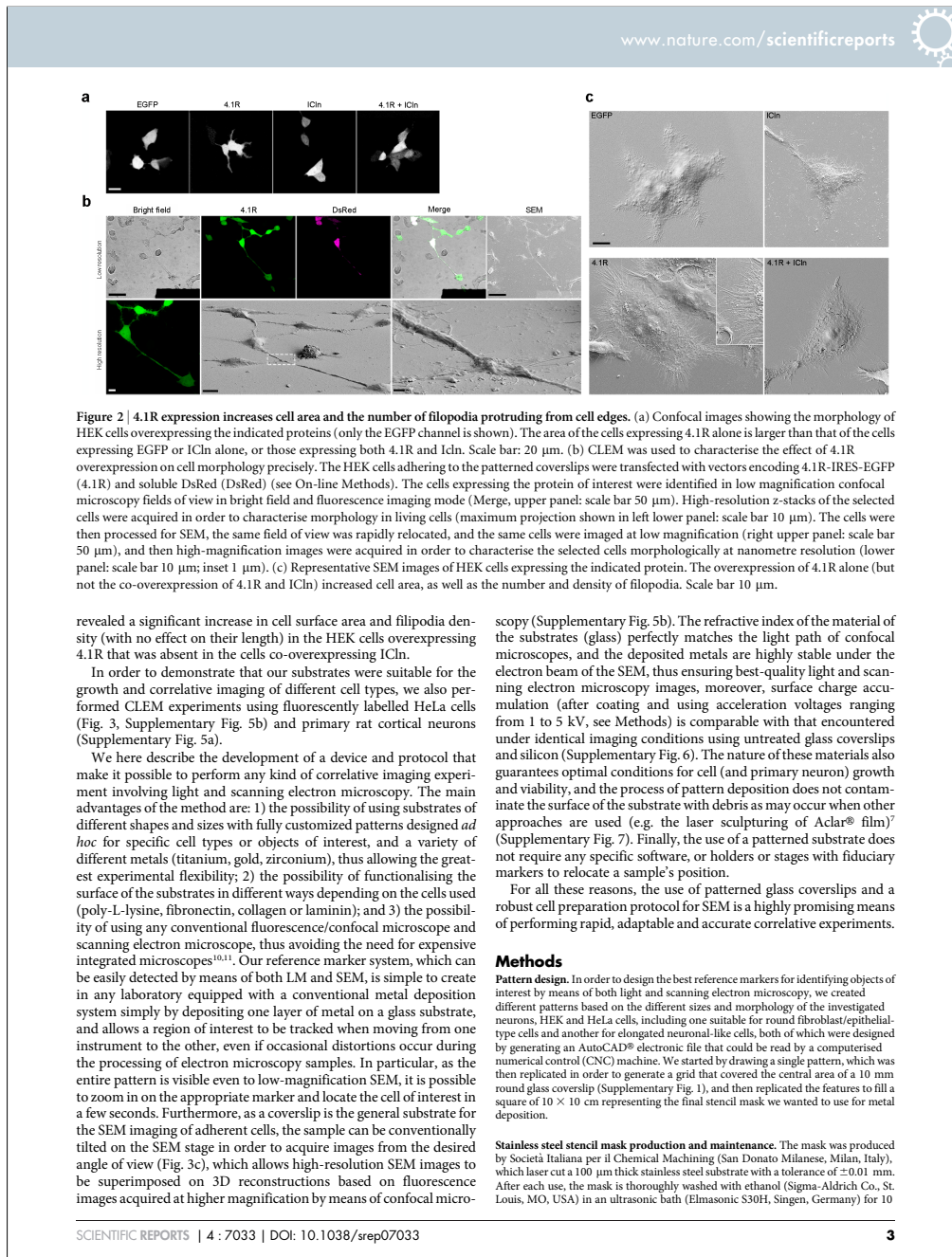


Figure 1 | Flow chart showing the process of creating a CLEM patterned glass coverslip and preparing the samples. (a) From pattern design to laser-cut mask. (b) Basic steps in creating a 10 mm diameter patterned glass coverslip. (c) Experimental protocol. The cells are seeded on an appropriately patterned, sterilized and functionalized glass coverslip before being transfected with constructs encoding the investigated and fluorescent proteins. Once the exogenous proteins are adequately expressed, the confocal microscopy images are acquired, and the samples are then fixed, immediately processed for SEM, and transferred to the SEM image acquisition chamber. The acquired images are finally analyzed to obtain the data of interest. Scale bars: 100 μm in the large confocal microscope and SEM large fields of view; 10 μm in the cell zooms; and 1 μm and 200 nm in the details.

5. APPENDIX



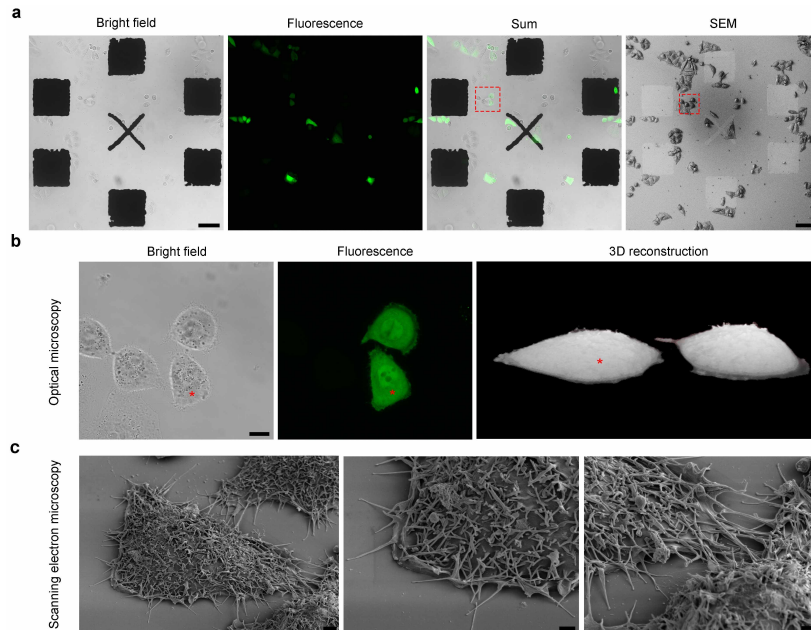


Figure 3 | High-resolution optical and electron microscopy images of HeLa cells expressing EGFP. (a) Fields of view showing HeLa cells overexpressing soluble EGFP growing on the patterned coverslip as acquired by means of optical microscopy (Bright field, Fluorescence and Sum) and SEM. Scale bars 100 μm . The pattern was developed so that it could be easily visualised by both microscopes in order to allow the rapid relocation of the same cells when moving from one to the other. (b) High-resolution optical images (Bright field and Fluorescence maximum projections), and a 3D reconstruction of the two EGFP-expressing cells (red box) in (a). Scale bar: 10 μm . (c) Scanning electron microscopy images of the EGFP-expressing HeLa cell asterisked in (b) showing the highly preserved ultrastructure obtained after SEM preparation on the patterned substrates, and the high-resolution details observable after tilting the sample holder. Scale bars 2 μm .

minutes and dried with nitrogen (N_2). This cleaning procedure is important to preserve the size of the features and guarantee reproducible electron beam metal deposition.

Generation of patterned coverslips by means of electron beam deposition. Before deposition, glass microscope coverslips with diameters of 10, 13, 15 and 24 mm (VWR International, Milan, Italy) were sonicated (Elmasonic S30H) in ethanol (Sigma-Aldrich Co.) and then in 2-propanol (Sigma-Aldrich Co.) for 30 minutes each, and dried with nitrogen (N_2). After being put into a coverslip holder with the mask for pattern generation (Fig. 1), they were loaded into a conventional custom-made evaporation system and the pressure inside the deposition chamber was brought to 6.0×10^{-6} mbar. The beam was switched on and set to a voltage of 6 kV, and the evaporation was started by gradually increasing the current to 34 mA, a value at which titanium (99.999% pure, Kurt J. Lesker, Hastings, UK) starts to melt, evaporate and deposit at a rate of 0.2 Å/sec. (the same deposition rate was also used for gold and zirconium but, given their different physical properties, it was necessary to use higher currents (respectively 420 mA and 165 mA) and longer deposition times). The film thickness and rate of deposition were controlled by means of a quartz crystal monitor. When the desired thickness was reached (100 nm in the case of titanium), the beam was switched off, the chamber was vented, and the substrates were removed ready to be used for the correlative experiments.

Sterilisation and functionalisation of the patterned coverslips. Before seeding the cells, the patterned coverslips were sterilized in a stove at 180 °C overnight and/or washed in ethanol 70% and/or exposed to UV radiation for 50 minutes, functionalized with a drop of poly-L-lysine solution 0.1% w/v in water (Sigma-Aldrich Co.) for five minutes, and then rinsed with bi-distilled water. For the experiments described in Supplementary Figure 6, the silicon substrates were

sonicated in acetone and isopropanol for 10 minutes, and sterilized using ethanol and UV radiation before being functionalized with poly-L-lysine 1 mg/ml.

Cell cultures. HeLa or human embryonic kidney (HEK) 293T cells were grown in Eagle's minimum essential medium (EMEM; 12-125F, Lonza® Walkersville, Inc., Walkersville, MD, USA) supplemented with 10% fetal bovine serum (FBS), L-glutamine 2 mM, non-essential amino acids 0.1 mM, penicillin 100 U, streptomycin 100 $\mu\text{g}/\text{ml}$, and sodium pyruvate 1 mM, and the cultures were maintained in a humidified incubator at 37 °C with 5% CO_2 .

The cells were split every 3–4 days when 80–90% confluent. Briefly, the culture medium was discarded, and the cell layer was rinsed with phosphate buffer saline (PBS: NaCl 136.89 mM, KCl 2.69 mM, Na_2PO_4 1.47 mM, NaOH 10 mM, pH 7.4) to remove all traces of serum, which contains trypsin inhibitor. Trypsin-EDTA 0.25% was added, and the culture dish was put in an incubator at 37 °C for five minutes, after which complete growth medium was added and the cells were dissociated by means of gentle pipetting. Appropriate aliquots of the cell suspension was added to new culture dishes, and the cultures were incubated again at 37 °C.

For the CLEM experiments, HeLa or HEK cells were seeded at a concentration of 160 cells/ mm^2 on the patterned coverslips functionalized with poly-L-lysine, and the cultures were incubated at 37 °C until cell adhesion.

After the patterned coverslips were cleaned with 100% ethanol at 37 °C for two hours, washed with sterilized H_2O , heated at 180 °C for five hours, functionalized with poly-L-lysine 1 mg/ml, and rinsed with water, rat hippocampal neurons were seeded on the substrates at a concentration of 160 cells/ mm^2 in Dulbecco's modified Eagle's medium (DMEM) supplemented with 10% FBS, L-glutamine 2 mM, non-essential amino acids 0.1 mM, penicillin 100 U, streptomycin 100 $\mu\text{g}/\text{ml}$, and sodium pyruvate 1 mM (all of the reagents were purchased from Life Technologies™, Monza, Italy).

5. APPENDIX

Plasmids. The 4.1R-IRES-GFP and IClN-IRES-dsRED vectors¹⁴, expressing the 4.1R135 or IClN proteins and the fluorescent protein as two distinct polypeptides, were a kind gift of Dr. Claudia Bazzini (University of Milan, Milan, Italy) and of Prof. Markus Paulmichl (Paracelsus Medical University, Salzburg, Austria), respectively. The empty vectors: pIRES2-EGFP and pIRES2-dsREDexpress were used as controls.

HEK and HeLa cells were transiently transfected 24 hours post-seeding. In the co-transfection experiments, each vector was equimolar in the transfection mix.

Neurons were transfected with pEYFP-C1 (Clontech Laboratories, Inc.® - St. Germain en Laye, France).

Transient transfection. The cell lines were transiently transfected using the calcium phosphate method, adding 1 µg DNA and 2.5 µl CaCl₂ 2.5 M (Sigma-Aldrich Co.) for each 1.6 cm dish, and distilled water to bring the total volume to 25 µl. After five minutes, 25 µl of HBS 2x (NaCl 140 mM, NaH₂PO₄ 1.5 mM, HEPES 50 mM, pH 7.05) were gently added to the CaCl₂/DNA mix, and the transfection mixture was then added dropwise to the cell culture. The dish was transferred to the incubator at 37 °C and 5% CO₂, and after 6–10 hours, the medium was replaced by warm complete medium and incubation resumed. The neurons were transfected after three days *in vitro* (DIV) using 3 µg of DNA and the same procedure as that described for the cell lines, and imaged on *in vitro* day 5.

MTT assay. HeLa cells were seeded at a concentration of 600 cells/mm² on 10 mm glass coverslips or patterned substrates that were sterilized with 70% ethanol and 50 minutes of UV radiation, and functionalized with poly-L-lysine 1 mg/mL. Twenty-four and 48 hours after seeding, the cells were incubated for four hours with the MTT solution (3-(4,5-dimethylthiazol-2-yl)-2,5-diphenyltetrazolium bromide, Cell Proliferation Kit I, Cat. No. 11465007001, Roche Diagnostic GmbH, Mannheim, Germany). After incubation, the purple formazan salt crystals were solubilised by adding the solubilisation solution and incubating the plates overnight in a humidified atmosphere (37 °C, 5% CO₂). The solubilised formazan product was spectrophotometrically quantified using an ELISA reader (Tecan Sunrise, Tecan Group Ltd., Männedorf, Switzerland). Cell viability was evaluated at each time point in four independent experiments for each substrate.

Confocal microscopy. Images of the cells on the patterned coverslips were acquired using a Leica TCS SP5 confocal inverted microscope (Leica Microsystems GmbH, Wetzlar, Germany) with an HCL PL.FLUOTAR 20×0.5 (NA 0.5) objective, a pixel size of 378.8 × 378.8 nm, and a scan speed of 400 Hz (low resolution/low magnification). EGFP was excited with a 488 nm laser line, and the PMT1 emission bandwidth was 500–550 nm; DsRED was excited with a 561 nm laser line, and the PMT2 emission bandwidth was 570–650 nm; EYFP was excited with a 514 nm laser line, and the PMT2 emission bandwidth was 525–600 nm; and the Hoechst nuclear dye was excited with a 405 nm laser line, and the PMT1 emission bandwidth was 415–455 nm. Bright field images were also acquired with the fluorescence channels superimposed (Imagel 1.45 software, Wayne Rasband, NIH, USA) in order to visualise the pattern together with the transfected and non-transfected cells on the coverslip. During confocal image acquisition, the cells were kept alive in the microscope incubator (Okolab, Naples, Italy) at 37 °C and 5% CO₂ in DPBS (PBS supplemented with CaCl₂ 1 mM, MgCl₂ 0.5 mM, and glucose 25 mM, pH 7.4).

The high-resolution images for the 3D reconstruction were acquired by means of an HCX PL APO 63×1.4 (NA 1.4) objective, a pixel size of 98.8 × 98.8 nm, and a z-step size of 250 nm using the same parameters as those described above. The 3D images were produced using the UCSF Chimera package from the Resource for Biocomputing, Visualization and Informatics at the University of California, San Francisco (supported by NIH P41 RR-01081) (Supplementary reference).

Cell adhesion analysis. HeLa cells were seeded at a concentration of 600 cells/mm² on 10 mm glass coverslips or patterned substrates that were sterilized with 70% ethanol and 50 minutes of UV radiation, and functionalized with poly-L-lysine 1 mg/mL. Twenty-four and 48 hours after seeding, the cells were fixed with 4% paraformaldehyde in PBS for 30 minutes, rinsed with PBS, incubated with Hoechst 33342 0.01 mg/mL (H1399, Molecular Probes®, Life Technologies Europe BV, Monza, Italy) for 30 minutes, and mounted in 90% glycerol. The density of the cells grown on the substrates was evaluated at each time point in four independent experiments for each substrate by counting the density of cell nuclei in fields of view (775 × 775 µm) acquired with the 20× objective of the confocal microscope using Imagel software. Both bright field and fluorescence images were recorded.

SEM sample preparation. The cells were processed for SEM imaging immediately after the acquisition of the confocal images. They were fixed with glutaraldehyde 1.2% in NaCacodylate 0.1 M for one hour, washed three times with NaCacodylate 0.1 M for 10 minutes, and post-fixed with osmium tetroxide (OsO₄) 1% in NaCacodylate 0.1 M for one hour. After removing the OsO₄ solution and rinsing twice with bi-distilled water, the samples were gradually dehydrated by means of an ethanol series, and then dried using an Emitech K850 critical point drier (Bad Schwalbach, Germany) or hexamethyldisilazane (HMDS). All of the reagents were purchased from Electron Microscopy Sciences (EMS, Hatfield, PA, USA). Once dried, the samples were sputtered with gold (Polaron E5100 Sputter Coater, Bad Schwalbach, Germany) and the images were acquired at 1–5 kV using a field emission gun scanning electron microscope (Zeiss, Oberkochen, Germany) with a secondary electron detector (SED). The samples for the experiments described in Supplementary Figure 6 were imaged before and after gold coating as described above.

Generation of the Aclar® patterned substrate for CLEM. A pattern with coordinates consisting of an asymmetrical mesh of squares of about 140 µm was sculpted on Aclar® film using the pulsed laser of a microdissecting microscope¹ (Leica Microsystems GmbH, Wetzlar, Germany). Before seeding the cells, each 10 mm Aclar® disc was sterilized using ethanol 70% and UV radiation for 50 minutes, and then functionalized with poly-L-lysine. The cells were cultured and transfected as described above.

1. Smith, C. Microscopy: Two microscopes are better than one. *Nature*. **492**, 293–297 (2012).
2. Sjollem, K. A., Schnell, U., Kuipers, J., Kalicharan, R. & Giepmans, B. N. G. Correlated light microscopy and electron microscopy. *Methods Cell Biol.* **3**, 157–173 (2012).
3. Zhang, P. Correlative cryo-electron tomography and optical microscopy of cells. *Curr Opin Struct Biol.* **23**, 763–770 (2013).
4. Spiegelhalter, C., Laporte, J. F. & Schwab, Y. Correlative light and electron microscopy: from live cell dynamic to 3D ultrastructure. *Methods Mol Biol.* **1117**, 485–501 (2014).
5. Agrawal, U., Reilly, D. T. & Schroeder, C. M. Zooming in on biological processes with fluorescence nanoscopy. *Curr Opin Biotechnol.* **24**, 646–653 (2013).
6. Villa, E., Schaffer, M., Plitzko, J. M. & Baumeister, W. Opening windows into the cell: focused-ion-beam milling for cryo-electron tomography. *Curr Opin Struct Biol.* **23**, 771–777 (2013).
7. Jiménez, N. et al. Gridded Aclar: preparation methods and use for correlative light and electron microscopy of cell monolayers, by TEM and FIB-SEM. *J Microsc.* **237**, 208–220 (2010).
8. Small, J. V. Simple procedures for the transfer of grid images onto glass coverslips for the rapid relocation of cultured cells. *Journal of Microscopy.* **137**, 171–175 (1985).
9. Powell, D. H. & Czymmek, K. J. A Low Cost Correlative Technique for Cell Imaging via Confocal and Scanning Electron Microscopy. *Microscopy and Microanalysis.* **15**, 940–941 (2009).
10. Liv, N. et al. Simultaneous correlative scanning electron and high-NA fluorescence microscopy. *PLoS One* **8** (2013).
11. Nishiyama, H. et al. Atmospheric scanning electron microscope system with an open sample chamber: Configuration and applications. *Ultramicroscopy* **147**, 86–97 (2014).
12. Depprich, R. et al. Behavior of osteoblastic cells cultured on titanium and structured zirconia surfaces. *Head Face Med.* **4**, 29 (2008).
13. Ozkucur, N. et al. Physical vapor deposition of zirconium or titanium thin films on flexible polyurethane highly support adhesion and physiology of human endothelial cells. *J Biomed Mater Res A.* **89**(1), 57–67 (2008).
14. Bazzini, C. et al. IClN: a new regulator of non-erythroid 4.1R localisation and function. *PLoS One* **9** (10), e108826. doi:10.1371/journal.pone.0108826 (2014).
15. An, X. Identification and functional characterization of protein 4.1R and actin-binding sites in erythrocyte beta spectrin: regulation of the interactions by phosphatidylinositol-4,5-bisphosphate. *Biochemistry.* **44**, 10681–10688 (2005).
16. Furst, J. et al. The IClN interactome. *Acta Physiol.* **187**, 43–49 (2006).

Acknowledgments

We would like to thank Cinzia Cagnoli who kindly provided the primary cortical neurons, and Gero Bongiorno for his helpful discussions during the first steps of substrate generation.

Author contributions

L.B. designed and carried out the cell cultures and CLEM protocols, and co-wrote the manuscript; E.S. designed and produced the patterned substrates, and co-wrote the manuscript; S.R. designed the fluorescence experiments and contributed to the pattern design; D.M. acquired the scanning electron microscopy images; P.M. supervised the project, and M.F. supervised the project and co-wrote the manuscript.

Additional information

Supplementary information accompanies this paper at <http://www.nature.com/scientificreports>

Competing financial interests: The authors declare no competing financial interests.

How to cite this article: Benedetti, L. et al. Customized patterned substrates for highly versatile correlative light-scanning electron microscopy. *Sci. Rep.* **4**, 7033; DOI:10.1038/srep07033 (2014).



This work is licensed under a Creative Commons Attribution 4.0 International License. The images or other third party material in this article are included in the article's Creative Commons license, unless indicated otherwise in the credit line; if the material is not included under the Creative Commons license, users will need to obtain permission from the license holder in order to reproduce the material. To view a copy of this license, visit <http://creativecommons.org/licenses/by/4.0/>

References

- [1] HUIHUI LI, SONGQIN LIU, ZHIHUI DAI, JIANCHUN BAO, AND XIAODI YANG. **Applications of nanomaterials in electrochemical enzyme biosensors.** *Sensors*, **9**(11):8547–8561, 2009.
- [2] EMIL RODUNER. **Size matters: why nanomaterials are different.** *Chemical Society Reviews*, **35**(7):583–592, 2006.
- [3] MOHAMMAD HASANZADEH, NASRIN SHADJOU, MIGUEL DE LA GUARDIA, MORTEZA ESKANDANI, AND PEYMAN SHEIKHZADEH. **Mesoporous silica-based materials for use in biosensors.** *TrAC Trends in Analytical Chemistry*, **33**:117–129, 2012.
- [4] SURESH SAGADEVAN AND MATHAN PERIASAMY. **Recent trends in nanobiosensor and their applications.** *Rev. Adv. Mater. Sci*, **36**:62–69, 2014.
- [5] SABAHUDIN HRAPOVIC, YALI LIU, KEITH B MALE, AND JOHN HT LUONG. **Electrochemical biosensing platforms using platinum nanoparticles and carbon nanotubes.** *Analytical chemistry*, **76**(4):1083–1088, 2004.
- [6] YUANYUANG LI, HERMANN J SCHLUESENER, AND SHUNQING XU. **Gold nanoparticle-based biosensors.** *Gold Bulletin*, **43**(1):29–41, 2010.
- [7] VASUDEVANPILLAI BIJU. **Chemical modifications and bioconjugate reactions of nanomaterials for sensing, imaging, drug delivery and therapy.** *Chemical Society Reviews*, **43**(3):744–764, 2014.
- [8] EDY WJAYA, CÉDRIC LENAERTS, SOPHIE MARICOT, JURIY HASTANIN, SERGE HABRAKEN, JEAN-PIERRE VILCOT, RABAH BOUKHERROUB, AND SABINE SZUNERITS. **Surface plasmon resonance-based biosensors: from the development of different SPR structures to novel surface functionalization strategies.** *Current Opinion in Solid State and Materials Science*, **15**(5):208–224, 2011.
- [9] XIAOWEI GUO. **Surface plasmon resonance based biosensor technique: A review.** *Journal of Biophotonics*, **5**(7):483–501, 2012.

REFERENCES

- [10] K LANCE KELLY, EDUARDO CORONADO, LIN LIN ZHAO, AND GEORGE C SCHATZ. **The optical properties of metal nanoparticles: the influence of size, shape, and dielectric environment.** *The Journal of Physical Chemistry B*, **107**(3):668–677, 2003.
- [11] ROBERT A REYNOLDS, CHAD A MIRKIN, AND ROBERT L LETSINGER. **Homogeneous, nanoparticle-based quantitative colorimetric detection of oligonucleotides.** *Journal of the American Chemical Society*, **122**(15):3795–3796, 2000.
- [12] WEI XU, XUEJIA XUE, TIANHU LI, HUAQIANG ZENG, AND XIAOGANG LIU. **Ultrasensitive and selective colorimetric DNA detection by nicking endonuclease assisted nanoparticle amplification.** *Angewandte Chemie International Edition*, **48**(37):6849–6852, 2009.
- [13] STEVEN J OLDENBURG, CHRISTINE C GENICK, KEITH A CLARK, AND DAVID A SCHULTZ. **Base pair mismatch recognition using plasmon resonant particle labels.** *Analytical Biochemistry*, **309**(1):109–116, 2002.
- [14] JUEWEN LIU AND YI LU. **Colorimetric biosensors based on DNAzyme-assembled gold nanoparticles.** *Journal of Fluorescence*, **14**(4):343–354, 2004.
- [15] XIAOXIAO HE, HAILING HUO, KEMIN WANG, WEIHONG TAN, PING GONG, AND JIA GE. **Plasmid DNA isolation using amino-silica coated magnetic nanoparticles (ASMNPs).** *Talanta*, **73**(4):764–769, 2007.
- [16] KANG LI, YANJUN LAI, WEN ZHANG, AND LITONG JIN. **Fe₂O₃ Au core/shell nanoparticle-based electrochemical DNA biosensor for *Escherichia coli* detection.** *Talanta*, **84**(3):607–613, 2011.
- [17] JI HYUN MIN, MI-KYUNG WOO, HA YOUNG YOON, JIN WOO JANG, JUN HUA WU, CHAE-SEUNG LIM, AND YOUNG KEUN KIM. **Isolation of DNA using magnetic nanoparticles coated with dimercaptosuccinic acid.** *Analytical Biochemistry*, **447**:114–118, 2014.
- [18] CR TAMANAHA, SP MULVANEY, JC RIFE, AND LJ WHITMAN. **Magnetic labeling, detection, and system integration.** *Biosensors and Bioelectronics*, **24**(1):1–13, 2008.
- [19] M MUJKA, S ARANA, E CASTANO, M TIJERO, R VILARES, JM RUANO-LOPEZ, A CRUZ, L SAINZ, AND J BERGANZA. **Magneto-resistive immunosensor for the detection of *Escherichia coli* O157: H7 including a microfluidic network.** *Biosensors and Bioelectronics*, **24**(5):1253–1258, 2009.
- [20] SUSANA LIEBANA, ANABEL LERMO, SUSANA CAMPOY, JORDI BARBÉ, SALVADOR ALEGRET, AND MARÍA ISABEL PIVIDORI. **Magneto immunoseparation of pathogenic bacteria and electrochemical magneto genosensing of the double-tagged amplicon.** *Analytical Chemistry*, **81**(14):5812–5820, 2009.

REFERENCES

- [21] ALESSIA BATTIGELLI, CÉCILIA MÉNARD-MOYON, TATIANA DA ROS, MAURIZIO PRATO, AND ALBERTO BIANCO. **Endowing carbon nanotubes with biological and biomedical properties by chemical modifications.** *Advanced Drug Delivery Reviews*, **65**(15):1899–1920, 2013.
- [22] CÉCILIA MÉNARD-MOYON, KOSTAS KOSTARELOS, MAURIZIO PRATO, AND ALBERTO BIANCO. **Functionalized carbon nanotubes for probing and modulating molecular functions.** *Chemistry & Biology*, **17**(2):107–115, 2010.
- [23] JOSEPH WANG. **Carbon-nanotube based electrochemical biosensors: A review.** *Electroanalysis*, **17**(1):7–14, 2005.
- [24] ALAN LE GOFF, MICHAEL HOLZINGER, AND SERGE COSNIER. **Enzymatic biosensors based on SWCNT-conducting polymer electrodes.** *Analyst*, **136**(7):1279–1287, 2011.
- [25] SUNIL K. ARYA, SHIBU SAHA, JAIME E. RAMIREZ-VICK, VINAY GUPTA, SHEKHAR BHANSALI, AND SURINDER P. SINGH. **Recent advances in ZnO nanostructures and thin films for biosensor applications.** *Analytica Chimica Acta*, **737**(0):1 – 21, 2012.
- [26] PRATIBHA PANDEY, MONIKA DATTA, AND BD MALHOTRA. **Prospects of nanomaterials in biosensors.** *Analytical Letters*, **41**(2):159–209, 2008.
- [27] SP SINGH, SUNIL K ARYA, PRATIBHA PANDEY, BD MALHOTRA, SHIBU SAHA, K SREENIVAS, AND VINAY GUPTA. **Cholesterol biosensor based on rf sputtered zinc oxide nanoporous thin film.** *Applied Physics Letters*, **91**(6):063901–063901, 2007.
- [28] JINPING LIU, YUANYUAN LI, XINTANG HUANG, AND ZHIHONG ZHU. **Tin oxide nanorod array-based electrochemical hydrogen peroxide biosensor.** *Nanoscale Research Letters*, **5**(7):1177–1181, 2010.
- [29] AJAY KUMAR GUPTA AND MONA GUPTA. **Synthesis and surface engineering of iron oxide nanoparticles for biomedical applications.** *Biomaterials*, **26**(18):3995–4021, 2005.
- [30] PRATIMA R SOLANKI, AJEET KAUSHIK, VED V AGRAWAL, AND BANSI D MALHOTRA. **Nanostructured metal oxide-based biosensors.** *NPG Asia Materials*, **3**(1):17–24, 2011.
- [31] HAN NIM CHOI, MIN AH KIM, AND WON-YONG LEE. **Amperometric glucose biosensor based on sol-gel-derived metal oxide/Nafion composite films.** *Analytica Chimica Acta*, **537**(1):179–187, 2005.
- [32] HANS M CHRISTEN AND GYULA ERES. **Recent advances in pulsed-laser deposition of complex oxides.** *Journal of Physics: Condensed Matter*, **20**(26):264005, 2008.

REFERENCES

- [33] ANNA MARIE LIPSKI, CLAUDE JAQUIERY, HOON CHOI, DANIEL EBERLI, MOLLY STEVENS, IVAN MARTIN, I-W CHEN, AND V PRASAD SHASTRI. **Nanoscale engineering of biomaterial surfaces.** *Advanced Materials*, **19**(4):553–557, 2007.
- [34] YI ZHAO CHEN, CAI TING YANG, CHI BUN CHING, AND RONG XU. **Immobilization of lipases on hydrophobilized zirconia nanoparticles: highly enantioselective and reusable biocatalysts.** *Langmuir*, **24**(16):8877–8884, 2008.
- [35] SONGQIN LIU, ZHIHUI DAI, HONGYUAN CHEN, AND HUANGXIAN JU. **Immobilization of hemoglobin on zirconium dioxide nanoparticles for preparation of a novel hydrogen peroxide biosensor.** *Biosensors and Bioelectronics*, **19**(9):963–969, 2004.
- [36] CHANGHUA LIU, YINGLI TENG, JING XU, YAJUAN YANG, AND ZONGFANG WU. **Amperometric biosensor for hydrogen peroxide based on immobilisation of haemoglobin on mesoporous zirconia.** *International Journal of Environmental Analytical Chemistry*, **91**(14):1367–1379, 2011.
- [37] NINGNING ZHU, AIPING ZHANG, QINGJIANG WANG, PINGANG HE, AND YUZHONG FANG. **Electrochemical detection of DNA hybridization using methylene blue and electro-deposited zirconia thin films on gold electrodes.** *Analytica Chimica Acta*, **510**(2):163–168, 2004.
- [38] G SUMANA, MAUMITA DAS, SAURABH SRIVASTAVA, AND BD MALHOTRA. **A novel urea biosensor based on zirconia.** *Thin Solid Films*, **519**(3):1187–1191, 2010.
- [39] YOUNG-SEON KO AND YOUNG-UK KWON. **Mesoporous Zirconia Thin Films with Three-Dimensional Pore Structures and Their Application to Electrochemical Glucose Detection.** *ACS Applied Materials & Interfaces*, **5**(9):3599–3606, 2013.
- [40] CHUNJING FENG, SHUANG DAI, AND LEI WANG. **Optical aptasensors for quantitative detection of small biomolecules: A review.** *Biosensors and Bioelectronics*, **59**:64–74, 2014.
- [41] YUNXIAN PIAO, DONG JU HAN, AND TAE SEOK SEO. **Highly conductive graphite nanoparticle based enzyme biosensor for electrochemical glucose detection.** *Sensors and Actuators B: Chemical*, **194**:454–459, 2014.
- [42] JIA ZHANG, YING SUN, BO XU, HUA ZHANG, YAN GAO, HANQI ZHANG, AND DAQIAN SONG. **A novel surface plasmon resonance biosensor based on graphene oxide decorated with gold nanorod-antibody conjugates for determination of transferrin.** *Biosensors and Bioelectronics*, **45**:230–236, 2013.
- [43] CRAIG TUERK AND LARRY GOLD. **Systematic evolution of ligands by exponential enrichment: RNA ligands to bacteriophage T4 DNA polymerase.** *Science*, **249**(4968):505–510, 1990.

REFERENCES

- [44] ANDREW D ELLINGTON AND JACK W SZOSTAK. **In vitro selection of RNA molecules that bind specific ligands.** *Nature*, **346**(6287):818–822, 1990.
- [45] XIAOYU PEI, JUN ZHANG, AND JIE LIU. **Clinical applications of nucleic acid aptamers in cancer.** *Molecular and clinical oncology*, **2**(3):341, 2014
- [46] YUAN WAN, YALING LIU, PETER B ALLEN, WASEEM ASGHAR, M ARIF IFTAKHER MAHMOOD, JIFU TAN, HOLLI DUHON, YOUNG-TAE KIM, ANDREW D ELLINGTON, AND SAMIR M IQBAL. **Capture, isolation and release of cancer cells with aptamer-functionalized glass bead array.** *Lab on a Chip*, **12**(22):4693–4701, 2012.
- [47] FELIPE OPAZO, MATTHEW LEVY, MICHELLE BYROM, CHRISTINA SCHÄFER, CLAUDIA GEISLER, TEJA W GROEMER, ANDREW D ELLINGTON, AND SILVIO O RIZZOLI. **Aptamers as potential tools for super-resolution microscopy.** *Nature Methods*, **9**(10):938–939, 2012.
- [48] KUN HAN, ZHIQIANG LIANG, AND NANDI ZHOU. **Design strategies for aptamer-based biosensors.** *Sensors*, **10**(5):4541–4557, 2010.
- [49] XIAOYU PEI, JUN ZHANG, AND JIE LIU. **Clinical applications of nucleic acid aptamers in cancer (Review).** *Molecular and clinical oncology*, **2**(3):341–348, 2014.
- [50] EDWARD N BRODY, MICHAEL C WILLIS, JONATHAN D SMITH, SUMEDHA JAYASENA, DOMINIC ZICHI, AND LARRY GOLD. **The use of aptamers in large arrays for molecular diagnostics.** *Molecular Diagnosis*, **4**(4):381–388, 1999.
- [51] ROBERT D JENISON, STANLEY C GILL, ARTHUR PARDI, AND BARRY POLISKY. **High-resolution molecular discrimination by RNA.** *Science*, **263**(5152):1425–1429, 1994.
- [52] YI-CHUNG CHANG, CHIA-YING YANG, RUEI-LIN SUN, YI-FENG CHENG, WEI-CHEN KAO, AND PAN-CHYR YANG. **Rapid single cell detection of *Staphylococcus aureus* by aptamer-conjugated gold nanoparticles.** *Scientific reports*, **3**:1863, 2013.
- [53] XIAOXIAO CAO, SHAOHUA LI, LIUCUN CHEN, HONGMEI DING, HUA XU, YANPING HUANG, JIE LI, NON-GLIE LIU, WEIHONG CAO, YANJUN ZHU, BEIFEN SHEN, AND NINGSHENG SHAO. **Combining use of a panel of ssDNA aptamers in the detection of *Staphylococcus aureus*.** *Nucleic Acids Research*, **37**(14):46214628, August 2009.
- [54] HIROYUKI UYEYAMA, MAKOTO TAKAGI, AND SHIGEORI TAKENAKA. **A novel potassium sensing in aqueous media with a synthetic oligonucleotide derivative. Fluorescence resonance energy transfer associated with guanine quartet-potassium ion complex formation.** *Journal of the American Chemical Society*, **124**(48):14286–14287, 2002.

REFERENCES

- [55] JOHN G BRUNO AND JOHNATHAN L KIEL. **In vitro selection of DNA aptamers to anthrax spores with electrochemiluminescence detection.** *Biosensors and Bioelectronics*, **14**(5):457–464, 1999.
- [56] GUSTAVO A ZELADA-GUILLÉN, JOSÉ LUIS SEBASTIÁN-AVILA, PASCAL BLONDEAU, JORDI RIU, AND F XAVIER RIUS. **Label-free detection of *Staphylococcus aureus* in skin using real-time potentiometric biosensors based on carbon nanotubes and aptamers.** *Biosensors and Bioelectronics*, **31**(1):226–232, 2012.
- [57] PASQUALE EMANUELE SCOPELLITI, ANTONIO BORGONOVO, MARCO INDRIERI, LUCA GIORGETTI, GERO BONGIORNO, ROBERTA CARBONE, ALESSANDRO PODESTÁ, AND PAOLO MILANI. **The Effect of Surface Nanometre-Scale Morphology on Protein Adsorption.** 01 2013.
- [58] LASMA GAILITE, PASQUALE EMANUELE SCOPELLITI, VIMAL KUMAR SHARMA, MARCO INDRIERI, ALESSANDRO PODESTÁ, GABRIELLA TEDESCHI, AND PAOLO MILANI. **Nanoscale roughness affects the activity of enzymes adsorbed on cluster-assembled titania films.** *Langmuir*, 2014.
- [59] GABRIELE CORBELLI, CRISTIAN GHISLERI, MATTIA MARELLI, PAOLO MILANI, AND LUCA RAVAGNAN. **Highly deformable nanostructured elastomeric electrodes with improving conductivity upon cyclical stretching.** *Advanced Materials*, **23**(39):4504–4508, 2011.
- [60] E BARBORINI, P PISERI, A LI BASSI, A.C FERRARI, C.E BOTTANI, AND P MILANI. **Synthesis of carbon films with controlled nanostructure by separation of neutral clusters in supersonic beams.** *Chemical Physics Letters*, **300**(56):633 – 638, 1999.
- [61] E. BARBORINI, P. PISERI, A. PODESTÁ, AND P. MILANI. **Cluster beam microfabrication of patterns of three-dimensional nanostructured objects.** *Applied Physics Letters*, **77**(7), 2000.
- [62] P. MILANI, P. PISERI, E. BARBORINI, A. PODESTÁ, AND C. LENARDI. **Cluster beam synthesis of nanostructured thin films.** *Journal of Vacuum Science Technology A*, **19**(4), 2001.
- [63] P. PISERI, A. PODESTÁ, E. BARBORINI, AND P. MILANI. **Production and characterization of highly intense and collimated cluster beams by inertial focusing in supersonic expansions.** *Review of Scientific Instruments*, **72**(5), 2001.
- [64] R. G. AGOSTINO, T. CARUSO, G. CHIARELLO, A. CUPOLILLO, D. PACILÈ, R. FILOSA, V. FORMOSO, E. COLAVITA, L. PAPAGNO, C. DUCATI, E. BARBORINI, C. LENARDI, G. BONGIORNO, P. PISERI, AND P. MILANI. **Thermal annealing and hydrogen exposure effects on cluster-assembled nanostructured carbon films embedded with transition metal nanoparticles.** *Phys. Rev. B*, **68**:035413, Jul 2003.

REFERENCES

- [65] A LAUSI, E Busetto, M LEONI, AND P SCARDI. **The MCX project: a Powder Diffraction beamline at ELETTRA.** *Synchrotron Radiation in Natural Science*, **5**(1-2):5, 2006.
- [66] PIETRO RIELLO, ANDREA LAUSI, JENNIFER MACLEOD, JASPER RIKKERT PLAISIER, GIULIO ZERAUSCHEK, AND PAOLO FORNASIERO. **In situ reaction furnace for real-time XRD studies.** *Journal of Synchrotron Radiation*, **20**(1):194–196, 2012.
- [67] AP HAMMERSLEY. **FIT2D: an introduction and overview.** *European Synchrotron Radiation Facility Internal Report ESRF97HA02T*, 1997.
- [68] AP HAMMERSLEY. **FIT2D V12. 012 Reference Manual V6. 0.** *ESRF International Report No. ESRF98HA01T. Program available at <http://www.esrf.eu/computing/scientific/FIT2D>*, 2004.
- [69] AC LARSON AND RB VON DREELE. **General Structure Analysis System (GSAS); Report LAUR 86-748; Los Alamos National Laboratory: Los Alamos, NM, 2000.** *There is no corresponding record for this reference.*
- [70] PASQUALE EMANUELE SCOPELLITI, GERO BONGIORNO, AND PAOLO MILANI. **High Throughput Tools for the Study of Protein-Nanostructured Surface Interaction.** *Combinatorial Chemistry High Throughput Screening*, **14**(3):206–216, 2011-03-01T00:00:00.
- [71] FRANCESCA TAVERNA, ARMANDO NEGRI, RENATA PICCININI, ALFONSO ZECCONI, SIMONA NONNIS, SEVERINO RONCHI, AND GABRIELLA TEDESCHI. **Characterization of cell wall-associated proteins of a *Staphylococcus aureus* isolated from bovine mastitis case by a proteomic approach.** *Veterinary Microbiology*, **119**(24):240 – 247, 2007.
- [72] MASAHIKO MORINAGA, H ADACHI, AND M TSUKADA. **Electronic structure and phase stability of ZrO_2 sub i 2 i /sub i .** *Journal of Physics and Chemistry of Solids*, **44**(4):301–306, 1983.
- [73] FARZIEN ZANDIEHNADEM, RA MURRAY, AND WY CHING. **Electronic structures of three phases of zirconium oxide.** *Physica B+ C*, **150**(1):19–24, 1988.
- [74] EUN JEONG CHO, JAMES R. COLLETT, ANNA E. SZAFRANSKA, AND ANDREW D. ELLINGTON. **Optimization of aptamer microarray technology for multiple protein targets.** *Analytica Chimica Acta*, **564**(1):82 – 90, 2006.
- [75] SATU T KORHONEN, MONICA CALATAYUD, AND A OUTI I KRAUSE. **Stability of Hydroxylated (111) and (101) Surfaces of Monoclinic Zirconia: A Combined Study by DFT and Infrared Spectroscopy.** *The Journal of Physical Chemistry C*, **112**(16):6469–6476, 2008.

REFERENCES

- [76] KYEONG TAEK JUNG AND ALEXIS T BELL. **The effects of synthesis and pretreatment conditions on the bulk structure and surface properties of zirconia.** *Journal of Molecular Catalysis A: Chemical*, **163**(1):27–42, 2000.

Acknowledgements

I would like to say thanks to my PhD advisor, Professor Paolo Milani, who gave me the possibility to discover, in these 4 years, new things regarding physics, biology and the “art” to make do with what you have available and with your own strength.

I say thanks to FONDAZIONE CARIPLO which economically supported my PhD project about the development of a sensor for the detection of *Staphylococcus aureus*, and Professor Maria Luisa Gelmi the coordinator of this tricky, but interesting, project.

In particular I have to mention people who helped me in the lab work: professor Gabriella Tedeschi, Elisa Maffioli and Fabiana Santagata, thank you for your help in the proteomic analysis...it is really a complicated world for me!!

Thanks to Arianna Gabrieli and Marco Toscano for teaching me how to take care of SAU, SEP and COLI, it is your fault if bacteria are now my best friends ;-)

Thanks to Margherita Tamplenizza who introduced me to the fancy world of cell culture...me and PC12 are really grateful!!

Thanks to Francesca Borghi for AFM characterization...and for having

shared with me joys and pains of nanomaterials..our Zirconia will conquer the world..one day..sooner or later :-p

Thanks to Caterina Ducati, University of Cambridge, Department of Materials Science and Metallurgy, for the HRTEM measurements and Marco Merlini, University of Milan, Dipartimento di Scienze della Terra “ARDITO DESIO” for the XRD measurements and analysis.

Thanks to Martin Vondracek, Institute of Physics Czech Academy of Science, Prague, for the help with XPS measurements at the Materials Science Beamline at ELETTRA synchrotron.

For the development of the CLEM device I have to thank Maura Francolini, head of Imaging Platform at FONDAZIONE FILARETE, for the fruitful discussions, Davide Marchesi for the SEM imaging, especially for the cells tilted images, they are really TOP :-) and Simona Rodighiero, the wizard of confocal microscopes, thanks also for your curious and precise approach to research.

Thanks to Gero who welcomed me at the very beginning of my PhD, when I still was unaware of PMCS (lucky days :-))!! I really cried tons of tears when you left the micro and nano platform..you were “The Guide” and the support. Thanks to PES (Pasquale Emanuele Scopelliti) for the good cheer and for the training..you also left the micro nano platform too soon. You both could have waited until my last PhD year..for sure I would have sworn less at PMCS, spotter and aptamers :-p

Thanks to Claudio Piazzoni who struggled with me at CIMaINa working on the PMCS..thanks to Lasma and Vimal, PhDs mate at Fondazione Filarete.

Lets switch to italian...

Marco, non ti ringrazieró per le tue super battute o per il tuo tono di voce super basso, ma ti ringrazieró per il richiamo alla colazione, alla pausa pranzo e alle merende del mattino e del pomeriggio..un orologio umano insomma :-), grazie anche per le spiegazioni scientifiche, le discussioni e per avermi sostenuta/sopportata in questi anni di condizione ufficio! Chantal: ultimo “acquisto” dell’ufficio..mi basterebbe dire: “tra ingegneri ci si capisce al volo, con uno sguardo” ..grazie per il tuo senso pratico, per il tuo buon umore, per le chiacchierate e per il cercare di essere il piú possibile ZEN, grazie per essere una degna spalla in fatto di marshmallow, cupcake, cheesecake, fritto, biliardino, aperitivi etc etc..e grazie anche a te per avermi sopportata nella fase eli-dottor Jekyll-Mr Hyde di scrittura tesi..Chiaretta: grazie per il tuo sostegno, per gli aperitivi in ufficio e fuori ufficio, per le chiacchierate serie e mica serie. Ele: grazie per aver condiviso con me parte di questo percorso “tortuoso”, so che comprendi gioie e dolori..grazie per le olive di nonna ed evviva i pigiama party!! Alfredo, grazie per le pause caffé in cui fai vedere il lato meno rose e fiori della vita riportandomi con i piedi per terra, per condividere i lati positivi e negativi del “potere della nanostruttura”, ne verremo a capo un giorno :-).

MV, Claudia, Simona: le super donne delle nanoparticelle..grazie anche a voi per essermi state vicine in questi anni, e sì Claudia, lo devo ammettere..un pochino-ino-ino mi mancherete :-p

E poi grazie a Ale, Fede, Irini, Laura, Smbat e Alexandra: chi per piú tempo chi per meno ha contribuito a farmi arrivare fin qui.

Marcella, Elena che dire: grazie ragazze, per le vostre risate, per i vostri suggerimenti biologichesì, per i caffè presi di corsa alla macchinetta e per i gossip :-p

BE-NE-DET-TI (LORI) compagna di avventure-sventure!! Grazie per avermi fatto scoprire IL BAFFO e il suo sbagliato (e vogliamo parlare dei panini?!?!?!), per le corse che non abbiamo mai fatto (giuro che mi ci ero messa d'impegno), per aver ascoltato i miei sfoghi e per esser stata un perfetto sostegno in questi anni!! Grazie per aver provato in tutti i modi a farmi capire cosa sia ICln (una proteina!?!?) e la sequenza IRES..grazie per avermi seguita passo passo nel mondo della microscopia correlativa..un giorno i nostri vetrini saranno in tutti i lab bio :-p.

WISE-people: Cristian, Mattia e Ale..grazie ragazzi per la vostra allegria, per i vostri progetti super-segreti che non mi avete voluto svelare, per i vostri canti e fischiettamenti alla PMCS che erano in grado di sovrastare il rumore di 4 pompe funzionanti al massimo e una porta ed arrivare fino all'ufficio :-). Grazie soprattutto a Marta!!! In questo caso devo ringraziare Elen (nome in codice N.d.A.) che ci ha fatto

conoscere. Ci siamo capite da subito, in te ho trovato davvero una persona su cui contare, che mi dice le cose come stanno senza troppi giri di parole!

Brivio, fratello, grazie!!! Per essere stato presente in questi anni, per avermi consigliata, ascoltata, a volte sgridata e per avermi ricordato che in fondo se son arrivata fin qui un po' il merito é anche mio.

Dani, compagna di avventure alla Scala, grazie per il sostegno e le discussioni sulla "vita" e sulla parte "leggera" della vita :-)

Gre, Edo, S8 compagni di viaggio in giro per il mondo: grazie per esserci e per la vostra voglia di partire per nuove avventure..la prossima Oman :-p ?

Alessio, So, Giu, Eli..compagni d'uni che si son trasformati in amici: il vostro sostegno mi ha aiutato ad arrivare fino qui e mi aiuterá a buttarmi a capofitto in nuove avventure!! Grazie davvero ragazzi!

Bolzon, Messi e MG..grazie, per la vostra presenza, per la vostra allegria, pazzia, capacità di ascoltare e capirmi con uno sguardo, di farmi ridere, di parlare di discorsi seri e poco seri, di sforzarvi di capire che cavolo stessi facendo durante questi 4 anni..ebbene, avrete ormai scoperto che non salveró il mondo :-p e nemmeno vinceró il nobel ma siete ancora al mio fianco quindi GRAZIEEEEE!!

Grazie a Veronica e Francesca, il cuore della SEMM, grazie per i vostri reminder, la vostra pazienza e per essere sempre stra-disponibili a qualsiasi richiesta!!

E infine, ma non per questo meno importanti, devo ringraziare i miei genitori..che mi hanno permesso di arrivare fino qua, il loro sostegno incondizionato (anche nei miei momenti di sconforto) e il loro sguardo critico verso ciò che ho fatto, faccio e faró mi ha fatto crescere, mi ha fatto tagliare traguardi che non pensavo di poter raggiungere e mi ha fatto mettere in discussione il mio modo di affrontare la vita e il lavoro. Grazie poi a mia sorella, Clod, mia prima fan :-), alle volte son stata intrattabile ma mi sei sempre stata vicina sapendo come prendermi, sappi che anche se lontane io ci saró sempre!!!

And thanks to you, stranger, who (maybe) decided to read my PhD thesis and these acknowledgments until the end..hope you enjoyed =)